

**How connectivity rules and synaptic properties shape the efficacy of pattern separation in the entorhinal cortex–dentate gyrus–CA3 network**

S. Jose Guzman<sup>1,2</sup>, Alois Schlögl<sup>1</sup>, Claudia Espinoza<sup>1,3</sup>, Xiaomin Zhang<sup>1,4</sup>, Benjamin A. Suter<sup>1</sup>, and Peter Jonas<sup>1,\*</sup>

1 IST Austria (Institute of Science and Technology Austria), Am Campus 1, A-3400 Klosterneuburg, Austria

2 Present address: Institute of Molecular Biotechnology (IMBA), Dr. Bohr-Gasse 3, A-1030 Wien, Austria

3 Present address: Medical University of Vienna (MUW) Austria, Division of Cognitive Neurobiology, Spitalgasse 4, A-1090 Wien, Austria

4 Present address: Brain Research Institute, University of Zürich, Winterthurerstrasse 190, CH-8057 Zürich, Switzerland

\* Corresponding author. E-mail: [peter.jonas@ist.ac.at](mailto:peter.jonas@ist.ac.at)

35 **Abstract**

36 **Pattern separation is a fundamental brain computation that converts small**  
37 **differences in input patterns into large differences in output patterns. Several**  
38 **synaptic mechanisms of pattern separation were proposed, including code**  
39 **expansion, inhibition, and plasticity. However, which of these mechanisms play a**  
40 **role in the entorhinal cortex (EC)–dentate gyrus (DG)–CA3 circuit, a classical**  
41 **pattern separation circuit, remains unclear. Here, we show that a biologically**  
42 **realistic, full-scale EC–DG–CA3 circuit model, including granule cells (GCs) and**  
43 **parvalbumin-positive inhibitory interneurons (PV<sup>+</sup>-INs) in the DG, is an efficient**  
44 **pattern separator. Both external gamma-modulated inhibition and internal lateral**  
45 **inhibition mediated by PV<sup>+</sup>-INs substantially contributed to pattern separation.**  
46 **Both local connectivity and fast signaling at GC–PV<sup>+</sup>-IN synapses were important**  
47 **for maximal effectiveness. Similarly, mossy fiber synapses with conditional**  
48 **detonator properties contributed to pattern separation. In contrast, perforant path**  
49 **synapses with Hebbian synaptic plasticity and direct EC–CA3 connection shifted**  
50 **the network towards pattern completion. Our results demonstrate that the**  
51 **specific properties of cells and synapses optimize higher-order computations in**  
52 **biological networks, and might be useful to improve the deep learning**  
53 **capabilities of technical networks.**

54

55 Key words: Pattern separation, GABAergic interneurons, PV<sup>+</sup> interneurons, lateral  
56 inhibition, granule cells, dentate gyrus, hippocampus, mossy fiber, winner-takes-all  
57 mechanism, network model, divergence and convergence, presynaptic plasticity, deep  
58 learning networks.

59

60

## 61 Introduction

62 A fundamental question in neuroscience is how higher-order computations are  
63 implemented at the level of synapses, neurons, and neuronal networks. A key  
64 computation in the brain is pattern separation, a process that converts slightly different  
65 synaptic input patterns into substantially different action potential (AP) output patterns<sup>1–</sup>  
66 <sup>4</sup>. Although pattern separation is a universal network computation conserved across  
67 circuits and species<sup>4</sup>, it is thought to play a particularly important role in the dentate  
68 gyrus (DG), the input region of the hippocampus in mammals<sup>5,6</sup>. A prevalent model of  
69 hippocampal memory suggests that pattern separation in the DG is essential for reliable  
70 storage and recall of memories in the downstream CA3 region<sup>2,7,8</sup>. Thus, analyzing the  
71 mechanisms of pattern separation is crucial for the understanding of both short-term  
72 processing and long-term storage of information.

73 Early models of pattern separation, inspired by the architecture of the  
74 cerebellum<sup>4,9,10</sup>, suggested that divergent feedforward excitation and code expansion  
75 play a role in pattern separation<sup>9</sup>. According to the Marr-Albus theory, projection from a  
76 small to a large population of neurons expands the dimensionality of coding space,  
77 increasing the separability of patterns by downstream biological decoders<sup>10</sup>. The Marr-  
78 Albus model is consistent with structural and functional connectivity rules of the  
79 cerebellum, because a single mossy fiber axon divergently projects onto ~600 granule  
80 cells (GCs)<sup>4</sup>. Whether code expansion also explains pattern separation in the rodent  
81 hippocampus, where ~50,000 entorhinal cortex (EC) neurons diverge to ~500,000 GCs,  
82 which re-converge onto ~200,000 CA3 pyramidal neurons<sup>11–13</sup>, is an open question.

83 More recent models of pattern separation implied an important role of lateral  
84 inhibition<sup>14</sup>. These models were supported by the synaptic organization of the olfactory  
85 system in insects<sup>15–17</sup>. In the mushroom body of the fly, a single inhibitory cell, the  
86 anterior paired lateral (APL) interneuron, plays a role in pattern separation. Activation of  
87 a single Kenyon cell activates the APL interneuron, which in turn provides powerful  
88 inhibition to all Kenyon cells<sup>16</sup>. Thus, global lateral inhibition mediated by the APL  
89 interneuron could implement a “winner-takes-all” mechanism, thereby establishing a  
90 powerful decorrelation algorithm<sup>18–20</sup>. Whether inhibition contributes to pattern

91 separation in the DG is less clear. Although lateral inhibition is uniquely abundant in the  
92 DG, multiple GCs need to fire APs to activate parvalbumin-positive inhibitory  
93 interneurons (PV<sup>+</sup>-INs) and to trigger lateral inhibition<sup>21,22</sup>. Furthermore, lateral inhibition  
94 is not global, but follows distance-dependent connectivity rules<sup>22</sup>. Thus, lateral inhibition  
95 cannot implement a winner-takes-all mechanism, although softer versions with multiple  
96 winners remain possible<sup>18,19,23</sup>.

97 The DG is connected to the downstream CA3 region via powerful mossy fiber  
98 synapses<sup>2,7</sup>. Whereas the DG seems to be specialized on pattern separation, the CA3  
99 region is traditionally associated with pattern completion<sup>8,24</sup>. How the pattern separation  
100 mechanism in the DG is integrated with the pattern completion function of the CA3  
101 region remains enigmatic. Furthermore, how the unique properties of hippocampal  
102 mossy fiber synapses, such as conditional and plasticity-dependent detonation<sup>25</sup>,  
103 contribute to pattern separation is unclear. Detonation properties of mossy fiber  
104 synapses may facilitate the transfer of information from the DG to CA3 region, which  
105 might contribute to pattern separation<sup>23</sup>. Furthermore, sparse mossy fiber connectivity  
106 will reduce correlations, which may enhance pattern separation<sup>26</sup>. Whether these rules  
107 hold in biologically realistic network models remains to be determined.

108 The DG receives its main input from the EC via the perforant path (PP)<sup>27</sup>.  
109 Hebbian plasticity at PP synapses could implement a competitive learning  
110 mechanism<sup>2,28,29</sup>, which might contribute to pattern separation. Consistent with this idea,  
111 genetic deletion of N-methyl-D-aspartate (NMDA)-type glutamate receptors in GCs  
112 reduces behavioral pattern separation<sup>30</sup>. However, plasticity at PP EC–GC synapses  
113 has also been suggested to contribute to pattern completion<sup>31</sup>, similar to its well-  
114 established function in the CA3 circuit<sup>8</sup>. As an additional complication, the PP not only  
115 projects to GCs in the DG, but also directly innervates the CA3 region<sup>32</sup>. In a simplified  
116 model, the relative strength of the mossy fiber and PP input onto CA3 pyramidal  
117 neurons determines the balance between decorrelated and original input<sup>23</sup>. However,  
118 whether this is also the case in a biologically realistic model remains unclear.

119 To address the mechanisms of pattern separation in the EC–DG–CA3 network,  
120 we developed a model based on experimentally determined cellular and synaptic

121 properties. Implementation in real size allowed us to analyze sparse coding regimes<sup>33</sup>  
122 and to insert measured connectivity rules<sup>22</sup>.

123

124

## 125 **Results**

### 126 **Pattern separation in a biologically realistic PN-IN network**

127 Pattern separation is a fundamental brain computation that converts small differences in  
128 input patterns into large differences in output patterns. The basic principle is illustrated  
129 in Extended Data Fig. 1. When two highly overlapping patterns (A and B) are applied at  
130 the input level of a neuronal population, two less overlapping patterns (A' and B') are  
131 generated at the output level (Extended Data Fig. 1a). Quantitatively, for any given pair  
132 of patterns, the correlation at the output ( $R_{\text{out}} = r(A', B')$ ) is smaller than that at the input  
133 ( $R_{\text{in}} = r(A, B)$ ) (Extended Data Fig. 1b). Thus, pattern separation may be graphically  
134 depicted in a plot of  $R_{\text{out}}$  against  $R_{\text{in}}$  for all pairs of patterns<sup>23</sup>. For an efficient pattern  
135 separation mechanism, the data points would be expected to be located below the  
136 identity line (Extended Data Fig. 1c). In contrast, for a pattern completion mechanism<sup>8</sup>,  
137 the data points will be above the identity line (Extended Data Fig. 1d).

138 To quantify the properties of the pattern separation circuit, we used three  
139 different measures (Methods). First, to describe the overall pattern separation  
140 performance, we defined an integral-based measure,  $\psi$ , computed as the area between  
141 the  $R_{\text{out}}-R_{\text{in}}$  data and the identity line, normalized by the maximal area (Extended Data  
142 Fig. 1e). Second, to selectively capture pattern separation performance within a region  
143 in which input patterns were highly similar, we defined a slope-based measure,  $\gamma$ ,  
144 computed as the slope of the  $R_{\text{out}}-R_{\text{in}}$  curve for  $R_{\text{in}} \rightarrow 1$  (Extended Data Fig. 1e, inset).  
145 Finally, to characterize the ability of the network to preserve rank similarity<sup>34-36</sup>, we  
146 computed a rank-based correlation coefficient  $\rho$  (Extended Data Fig. 1f). These three  
147 parameters describe complementary aspects of pattern separation. For example,

148 randomization is well known to decorrelate patterns (increasing the values of  $\psi$  and  $\gamma$ ),  
149 but fails to maintain similarity relations (decreasing the value of  $\rho$ ).

150 To explore whether a biologically realistic network is capable of pattern  
151 separation, we developed a model of the EC–DG–CA3 network based on empirical  
152 experimental data (Fig. 1; Supplementary Fig. 1; Supplementary Table 1;  
153 Supplementary Software). The network was created in full scale<sup>12,13</sup>. Both PN–IN  
154 connectivity in the DG and GC–CA3 connectivity was constrained by experimental  
155 data<sup>21,22,37</sup>. Similarly, GC–CA3 connectivity via mossy fibers was experimentally  
156 constrained<sup>11,25,38–40</sup>. As gamma oscillations show maximal power in the DG<sup>41,42</sup>, a  
157 corresponding phasic inhibitory conductance was simulated in GCs at the onset of each  
158 simulation epoch<sup>19</sup>. The model allowed us to simulate the activity in GCs, PV<sup>+</sup>-INs, and  
159 CA3 pyramidal neurons in a biologically realistic network and to examine how  
160 biophysical properties of synapses and functional connectivity rules affect pattern  
161 separation (Fig. 1b).

162 We then analyzed pattern separation at multiple levels of the network. For the  
163 biologically realistic standard parameters (Supplementary Table 1), the integral-based  
164 pattern separation measure  $\psi$  was 0.56 for the EC–DG component (Fig. 1c), 0.38 for  
165 the DG–CA3 component (Fig. 1d), and 0.80 for the entire EC–CA3 network (Fig. 1e).  
166 Thus, pattern separation was primarily generated in the EC–DG layer, but further  
167 amplified in the DG–CA3 layer. Values of the slope-based pattern separation measure  
168  $\gamma$  closely paralleled values of  $\psi$  (EC–DG:  $\gamma = 11.1$ ; DG–CA3:  $\gamma = 3.0$ ; EC–CA3:  $\gamma = 23.7$ ).  
169 Thus, the model was able to convert small differences at the input level into large  
170 differences at the output level. Finally, the rank-based pattern separation measure  $\rho$   
171 was high in the individual layers, as well as across the entire network (EC–DG:  $\rho = 0.98$ ;  
172 DG–CA3:  $\rho = 0.96$ , and EC–CA3:  $\rho = 0.94$ ; Fig. 2f–h). Thus, the biologically realistic  
173 full-scale network model accurately maintained similarity relations. These conclusions  
174 were unaffected by the details of model implementation (Supplementary Figs. 2–8;  
175 Methods).

176

## 177 **Pattern separation by gamma rhythm and lateral inhibition**

178 The finding that pattern separation accumulated in a multi-layer deep network-like  
179 architecture was surprising, given that the divergence–convergence properties of the  
180 circuit seemed inconsistent with a code expansion model<sup>9,10</sup>. To explore alternative  
181 mechanisms of pattern separation, we examined the contribution of inhibition (Fig. 2)<sup>4,9</sup>.  
182 It has been suggested that both external gamma-modulated inhibition and internal  
183 lateral inhibition contribute to pattern separation<sup>14,18,19,43,44</sup>. We therefore explored  
184 gamma-modulated inhibition and lateral inhibition, in isolation as well as in combination,  
185 for a suprathreshold excitatory drive to GCs ( $I_{\mu} = 1.8$  relative to threshold). Deletion of  
186 gamma-modulated external inhibition from the network model ( $J_{\text{gamma}} = 0$ ) reduced  $\psi$   
187 and  $\gamma$  over a wide range of excitatory synaptic drive (Fig. 2b, top right). In contrast,  
188 deletion of lateral inhibition reduced the range of excitatory drive in which both high  $\psi$   
189 and  $\rho$  could be achieved (Fig. 2b, bottom left). Thus, gamma inhibition and lateral  
190 inhibition differentially affected pattern separation. Elimination of both forms of inhibition  
191 substantially impaired pattern separation (Fig. 2b, bottom right). Thus, the combination  
192 of gamma-modulated inhibition and lateral inhibition provides a major contribution to  
193 separation mechanism in the model.

194 To further analyze the complex interaction of tonic excitatory drive, gamma-  
195 modulated inhibition, and lateral inhibition, we computed  $\psi$ – $I_{\mu}$ – $J_{\text{gamma}}$  contour plots (Fig.  
196 2c, d). With intact lateral inhibition, efficient pattern separation ( $\psi > 0.5$ ) was robustly  
197 observed in a wide region of the parameter space (Fig. 2c). In contrast, after deletion of  
198 lateral inhibition, efficient pattern separation was only detected within a narrow band in  
199 the  $I_{\mu}$ – $J_{\text{gamma}}$  parameter space, in which the amplitude of gamma-modulated inhibition  
200 precisely matched that of the excitatory drive (Fig. 2d). Thus, a simple thresholding  
201 mechanism combined with gamma-modulated inhibition was not sufficient to generate  
202 robust pattern separation.

203 Finally, we explored how interfering with lateral inhibition at multiple levels affects  
204 pattern separation (Fig. 2e–g). Reducing the peak connectivity of either excitatory E–I or  
205 inhibitory I–E connections ( $c_{E-I}$  and  $c_{I-E}$ ) markedly affected the efficacy of pattern

206 separation (Fig. 2e, light blue bars). Similarly, reducing the connectivity width of either  
207 excitatory E–I or inhibitory I–E connections ( $\sigma_{E-I}$  and  $\sigma_{I-E}$ ) reduced the efficacy of  
208 pattern separation (Fig. 2f). Finally, reducing the strength of either excitatory E–I or  
209 inhibitory I–E connections ( $J_{E-I}$  or  $J_{I-E}$ ) substantially decreased the efficacy of pattern  
210 separation (Fig. 2g). Thus, interfering with disynaptic inhibition at multiple levels  
211 uniformly inhibited pattern separation. Taken together, the combination of gamma  
212 oscillations and lateral inhibition plays a critical role in the pattern separation process in  
213 the DG.

214

### 215 **Moderate effects of divergent connectivity**

216 To systematically explore how divergence and convergence affect pattern separation,  
217 we first examined pattern separation in simple models, in which convergent or divergent  
218 connectivity was concatenated with a thresholding mechanism (Fig. 3a–d). In this  
219 simple model, the number of neurons and the degree of convergence and divergence  
220 could be freely varied. In our simulations, we changed the connectivity ratio from 1 : 10  
221 (divergence) to 10 : 1 (convergence). In contrast to our expectations, the degree of  
222 pattern separation, as quantified by  $\psi$ , was only slightly dependent on the connectivity  
223 ratio (Fig. 3c, d). Weak dependence on the connectivity ratio was observed over a wide  
224 range of activity values (Fig. 3d). Thus, divergent connectivity was not strictly required  
225 for pattern separation.

226 Next, we determined how convergence and divergence affected pattern  
227 separation in the full-scale, biologically realistic network model (Fig. 3e–g). To address  
228 this aspect, we varied the number or activity level of entorhinal cells ( $n_{EC}$  or  $\alpha_{EC}$ ), and  
229 peak value or width of EC-GC connectivity ( $\rho_{EC-GC}$  or  $\sigma_{EC-GC}$ )<sup>27,32,45</sup>. Increasing the  
230 number of ECs decreased  $\psi$ , whereas decreasing the number increased it (Fig. 3f, top).  
231 Similarly, increasing EC activity consistently decreased  $\psi$  (Fig. 3f, bottom). Changing  
232 EC–GC connection probability had more complex effects, with lowest values of  $\psi$  for  
233 intermediate connectivity, and highest values at both low- and high-connectivity limit  
234 (Fig. 3g, top). Finally, increasing EC–GC connection width consistently decreased  $\psi$

235 (Fig. 3g, bottom). Thus, the excitatory EC–GC connectivity only moderately influenced  
236 pattern separation. These results indicate that divergent connectivity was not strictly  
237 required for pattern separation, neither in a simplified model, nor in a biologically  
238 realistic full-scale network.

239

#### 240 **Requirement for local connectivity and fast PV<sup>+</sup>-IN signaling**

241 Classical models suggest that global PN–IN connectivity supported pattern separation  
242 more effectively than local connectivity<sup>9</sup>. However, our results indicate that a model  
243 based on local connectivity rules<sup>22</sup> is a highly efficient pattern separator. To resolve this  
244 apparent contradiction, we explored the effects of local E–I and I–E connectivity in the  
245 network model (Fig. 4a–c). To address the effects of locality in isolation, we maintained  
246 the total connectivity (i.e. the area under the connection probability–distance curve)  
247 through compensatory changes in maximal connection probability. Increasing the width  
248 of connectivity for either excitatory E–I or inhibitory I–E synaptic connections reduced  $\psi$ ;  
249 particularly large changes were observed when local connectivity was replaced by  
250 global random connectivity (Fig. 4b). Thus, local PN–IN connectivity supported pattern  
251 separation more effectively than global connectivity.

252 Next, we examined the effects of changes in the width of excitatory E–I and  
253 inhibitory I–E connectivity (Fig. 4c). As before, the total connectivity was maintained  
254 through compensatory changes in maximal connection probability. Contour plot analysis  
255 corroborated that local connectivity supported pattern separation more effectively than  
256 broad connectivity. However, the effects of changes in the width of excitatory E–I and  
257 inhibitory I–E connectivity were asymmetric. If focal E–I and I–E connectivity were  
258 equally important,  $\psi$  contour lines should have a slope of  $-1$ . However, contour lines  
259 were much steeper (Fig. 4c). Hence, local excitatory E–I connectivity (plotted on the  
260 abscissa) was more important for pattern separation than local inhibitory I–E  
261 connectivity (plotted on the ordinate). Thus, the biological connectivity scheme, in which  
262 excitatory E–I is narrower than inhibitory I–E connectivity<sup>22</sup>, is highly suitable for pattern  
263 separation.

264 Why does local connectivity support pattern separation better than global  
265 connectivity? Effects of local connectivity might be a consequence of changes in  
266 average latency, which are shorter in a locally connected network than in an equivalent  
267 random network (Fig. 4d). To test this hypothesis, we first examined the effects of  
268 changes in axonal propagation velocity. As predicted, decreases in both  $v_{AP\ E-I}$  and  $v_{AP\ I-E}$   
269 negatively affected pattern separation (Supplementary Fig. 9a). Next, we changed  
270 the connectivity width while maintaining the average kinetic properties of disynaptic  
271 inhibition through compensatory changes of  $v_{AP\ E-I}$  and  $v_{AP\ I-E}$  (Supplementary Fig. 9b).  
272 Changes in propagation velocity almost completely compensated the effects of changes  
273 in connectivity. Thus, local connectivity improved pattern separation through facilitation  
274 of rapid signaling.

275 If local connectivity enhanced pattern separation by increasing the average  
276 speed of lateral inhibition, other fast signaling processes in INs may also contribute<sup>21,46–</sup>  
277 <sup>48</sup>. To test this hypothesis, we systematically varied the corresponding model  
278 parameters (Fig. 4e, f). Increasing the synaptic delay at both excitatory GC–PV<sup>+</sup>-IN  
279 synapses and inhibitory PV<sup>+</sup>-IN–GC synapses impaired pattern separation (Fig. 4e).  
280 Notably, the effect was stronger than that of AP propagation velocity (Supplementary  
281 Fig. 9a). Similarly, prolonging the time constants of the synaptic currents at excitatory  
282 GC–PV<sup>+</sup>-IN synapses reduced pattern separation efficacy (Fig. 4f, top). Finally, slowing  
283 the membrane time constant of the PV<sup>+</sup>-INs inhibited pattern separation (Fig. 4f,  
284 bottom). Thus, the fast signaling properties of PV<sup>+</sup>-INs contributed to the efficacy of  
285 pattern separation process.

286

### 287 **Contribution of mossy fiber synapses to pattern separation**

288 In our standard model, the mossy fiber synapse between GCs and CA3 pyramidal  
289 neurons provides a significant contribution to pattern separation (Fig. 1c–e). In the  
290 model, we realistically implemented both connectivity and synaptic strength of mossy  
291 fiber synapses. The number of mossy fiber synapses per GC was taken at 15,  
292 consistent with previous morphological data<sup>11,22,38</sup>. The strength of hippocampal mossy

293 fiber synapses was assumed as subthreshold (with a synaptic strength / threshold ratio  
294 = 0.34), in agreement with previous experimental data showing that mossy fiber  
295 synapses have subthreshold properties under control conditions<sup>25,39,40,49</sup>.

296 How does sparse connectivity of hippocampal mossy fiber synapses contribute  
297 to pattern separation? Whereas dense connectivity may introduce correlations, sparse  
298 connectivity may avoid such correlations<sup>26</sup>. To test this hypothesis, we varied the  
299 number of mossy fiber terminals per axon (Fig. 5a–d). To maintain the activity level of  
300 the network, the individual synaptic conductance values were appropriately scaled.  
301 Unexpectedly, increasing the number of mossy fiber boutons per axon increased the  
302 amount of pattern separation in the second layer of the network. The pattern separation  
303 index  $\psi$ , measured between DG and CA3, increased from 0.37 to 0.61 (Fig. 5c, d).  
304 Similarly,  $\psi$  measured across the entire network increased from 0.80 to 0.92. Thus, the  
305 sparse connectivity of the mossy fiber synapse decreases, rather than increases, the  
306 magnitude of pattern separation (Fig. 5d).

307 A hallmark property of mossy fiber synapses is the unique extent of presynaptic  
308 plasticity, including facilitation, PTP, and long-term potentiation (LTP)<sup>25,40,50</sup>. To examine  
309 how these specific plasticity properties influence pattern separation, we systematically  
310 shifted synaptic strength in the range from the subdetonation into the detonation range  
311 (Fig. 5e, f). When synaptic strength relative to threshold was increased from 0.34 to  
312 0.51 and 1.01, the pattern separation index  $\psi$ , measured between DG and CA3,  
313 became progressively reduced ( $\psi = 0.38, 0.23, \text{ and } 0.07$ , respectively; Fig. 5e, top; Fig.  
314 5f). Similarly,  $\psi$  measured across the entire network became smaller ( $\psi = 0.80, 0.70,$   
315 and  $0.58$ , respectively; Fig. 5e, bottom; Fig. 5f). Thus, presynaptic plasticity at  
316 hippocampal mossy fiber synapses shifted the network from strong to weak pattern  
317 separation, that is, in the direction of pattern completion (Fig. 5f).

318

319 **Contribution of PP synapses to pattern completion**

320 The role of Hebbian plasticity at PP EC–GC synapses in pattern separation has been  
321 unclear<sup>30,31</sup>. To test the effects of Hebbian synaptic plasticity at PP synapses on pattern  
322 computations in the network, we initially simulated the responses of the network to 100  
323 EC patterns with the default parameter set in a control run, potentiated the PP EC–GC  
324 synapses according to a simple Hebbian synaptic plasticity rule, and subsequently  
325 simulated the responses of the network to 100 EC patterns with the potentiated  
326 synapses in a test run (Fig. 6a–c). Whereas the network demonstrated robust pattern  
327 separation under control conditions, potentiation according to a Hebbian plasticity rule  
328 reduced both the integral-based pattern separation index  $\psi$  and the slope-based index  
329  $\gamma$ , switching the network from a pattern separation into a pattern completion mode (Fig.  
330 6a–c).

331 PP inputs not only innervate GCs<sup>27</sup>, but also CA3 pyramidal neurons via PP  
332 EC–CA3 synapses<sup>32</sup>. Do these synapses also regulate pattern separation in the EC–  
333 DG–CA3 network? To address this question, a tonic excitatory drive computed from the  
334 EC activity and the EC–GC connectivity was applied in parallel to GCs and CA3  
335 pyramidal neurons after appropriate scaling to represent feedforward excitation.  
336 Increasing the strength of the PP EC–CA3 synapses markedly reduced the degree of  
337 pattern separation (Fig. 6d–f). Taken together, our results indicate that mossy fiber GC–  
338 CA3 synapses and PP EC–CA3 synapses synergistically regulate pattern computations,  
339 shifting the EC–DG–CA3 network from pattern separation in the direction of pattern  
340 completion.

341

## 342 **Discussion**

343 A fundamental question in neuroscience is how higher-order computations are  
344 implemented at the level of synapses, neurons, and neuronal networks. Our full-size,  
345 realistic network model provides an answer to this question, at least for a specific  
346 network function (pattern separation) and a specific circuit (the EC–DG–CA3 circuit).  
347 This information may be useful to expand the deep learning capabilities of technical  
348 networks<sup>51</sup>.

349 According to the Marr-Albus theory, divergence of excitatory connections plays a  
350 major role in pattern separation<sup>4,9,10,52</sup>. However, in the trisynaptic pathway, divergence  
351 at EC–GC synapses is followed by convergence at GC–CA3 pyramidal neuron  
352 synapses. How is pattern separation possible under these conditions? As the mossy  
353 fiber synapse is below the threshold of AP initiation in postsynaptic CA3 cells<sup>25</sup>,  
354 convergence followed by thresholding will establish a decorrelation mechanism<sup>15,53</sup>.  
355 Pattern separation in the mossy fiber system will accumulate with pattern separation  
356 generated in the DG, leading to increase of  $\psi$  across layers. Thus, pattern separation is  
357 not strictly localized to the DG, but represents a distributed network computation that  
358 involves multiple regions of the trisynaptic circuit.

359 Thresholding is a well-established decorrelation mechanism<sup>15,53,54</sup>. Consistent  
360 with the idea that thresholding contributes to pattern separation in the DG, GCs show a  
361 uniquely negative resting membrane potential and a high relative voltage threshold<sup>55</sup>.  
362 While our results confirm that thresholding in the complete absence of inhibition can  
363 result in pattern separation, efficient pattern separation is only possible in a narrow  
364 region of the parameter space. Addition of lateral inhibition markedly expands the  
365 regime of efficient pattern separation (Fig. 2c, d). This is consistent with behavioral  
366 experiments, which showed that both genetic deletion of GABA<sub>A</sub> receptors in GCs and  
367 pharmacogenetic inhibition of GABAergic INs in the DG affect pattern separation<sup>56,57</sup>.

368 Both experimental and theoretical evidence suggest that network oscillations,  
369 particularly in the gamma frequency range, may play a role in pattern separation<sup>19,58</sup>.  
370 We have incorporated gamma activity as a transient inhibitory conductance at the  
371 simulation onset, and found that this conductance enhanced pattern separation. It is  
372 possible that gamma oscillations and pattern separation are different reflections of the  
373 same phenomenon, e.g. disynaptic inhibition. Alternatively, gamma oscillations in the  
374 DG may be generated by mutual inhibition<sup>37,59</sup>. In this scenario, rhythmic gamma activity  
375 may assist pattern separation by structuring activity in time<sup>58</sup>. Thus, mutual inhibition  
376 and recurrent inhibition may cooperate to provide an optimal framework for pattern  
377 separation.

378           Several theories assume that global lateral inhibition plays a key role in pattern  
379 separation<sup>4,9</sup>. Intuitively, global inhibition could implement a “winner-takes-all” or a “k-  
380 winners-take-all” mechanism<sup>14,18,19,43,44</sup>. In the DG, lateral inhibition is abundant, but  
381 follows local distance-dependent connectivity rules<sup>22</sup>. How can a local lateral inhibition  
382 mechanism contribute to pattern separation? Unexpectedly, our model reveals that local  
383 connectivity supports pattern separation, even more effectively than global connectivity.  
384 The beneficial effects of local connectivity are almost completely compensated by  
385 reducing the signaling speed. Thus, local connectivity enhances pattern separation  
386 through a gain in the speed of lateral inhibition.

387           Fast signaling is a hallmark of function of GABAergic INs, particularly fast  
388 spiking, PV<sup>+</sup> subtypes<sup>46</sup>. Fast signaling properties are expressed at multiple levels,  
389 including excitatory synaptic input<sup>21,22</sup>, input-output transformation<sup>47</sup>, axonal AP  
390 propagation<sup>60</sup>, and inhibitory synaptic output<sup>48</sup>. However, the impact of these specific  
391 signaling properties on higher-order computations in neuronal networks is unclear.  
392 Here, we show that several fast signaling properties of GABAergic INs facilitate pattern  
393 separation. Short synaptic delays are particularly critical for pattern separation,  
394 suggesting that tight coupling between presynaptic Ca<sup>2+</sup> channels and release sensors  
395 might be important<sup>61</sup>. Furthermore, the decay time constant of the excitatory synaptic  
396 conductance at PN–IN synapses affects pattern separation, implying that the subunit  
397 composition of postsynaptic  $\alpha$ -amino-3-hydroxy-5-methyl-4-isoxazolepropionic acid  
398 (AMPA)-type glutamate receptors in INs is relevant. Thus, both pre- and postsynaptic  
399 molecular and subcellular specializations of PN–IN synapses contribute to the pattern  
400 separation at the network level.

401           Our model provides clues how the mossy fiber synapse contributes to pattern  
402 separation<sup>23,62</sup>. Pattern separation is not only relayed to the CA3 region, but rather  
403 conditionally amplified by the mossy fiber–CA3 synaptic connections (Fig. 1d, e; Fig. 5).  
404 The degree of amplification is determined by the properties of the synapse.  
405 Subdetonation properties will increase pattern separation, while detonation will reduce  
406 it. Previous work showed that the efficacy of mossy fiber synapses can be regulated by  
407 presynaptic plasticity mechanisms, which increase synaptic strength by almost an order

408 of magnitude<sup>25,40</sup>. This suggests that mossy fiber plasticity might tune the balance  
409 between pattern separation and pattern completion. As a corollary, bursts or  
410 superbursts in GCs may shift the network from strong to weaker pattern separation, i.e.  
411 in the direction of pattern completion<sup>33,40</sup>.

412 Hebbian synaptic plasticity is a hallmark property of PP EC–CA3 synapses<sup>28,29</sup>.  
413 Our results suggest that PP plasticity switches the network from pattern separation to  
414 completion. This may seem counter-intuitive, since a Hebbian rule based on presynaptic  
415 (original) patterns and postsynaptic (decorrelated) patterns might represent a feedback  
416 signal amplifying decorrelation<sup>15</sup>. However, in our simulations we applied 100 patterns  
417 with various degree of overlap. As plasticity induction requires multiple pre-post  
418 pairings, this preferentially strengthens the overlapping synapses, leading to an  
419 increase of correlation. Thus, whereas lateral inhibition consistently mediates pattern  
420 separation, PP plasticity may, at least with the chosen induction rules, promote pattern  
421 completion<sup>31</sup>. As a corollary, inhibition-based pattern separation could dominate at early  
422 time points (i.e. with novel patterns), whereas plasticity-based pattern completion may  
423 prevail later (i.e. with familiar patterns).

424 PP inputs not only innervate GCs, but also CA3 pyramidal neurons via PP EC–  
425 CA3 synapses<sup>32</sup>. In a simplified model, the mossy fiber pathway conveys decorrelated  
426 patterns, whereas the PP input relays the original patterns to postsynaptic CA3 cells<sup>23</sup>.  
427 The effects of the excitatory drive from the EC–CA3 synapses are consistent with this  
428 idea. However, our analysis further suggests that increasing the EC–CA3 drive reduces  
429 the contribution of the mossy fiber synapses to the total pattern separation process (Fig.  
430 6f). Intuitively, the EC–CA3 drive regulates the detonator properties of the mossy fiber–  
431 CA3 synapses by changing the effective firing threshold. Thus, complex interactions  
432 between excitatory and inhibitory synapses regulate the balance between pattern  
433 separation and completion.

434 Our biologically inspired network model is an efficient pattern separator.  
435 However, the network also may be able to perform other related higher-order  
436 computations. The pattern separation reliability  $\rho$  is close to 1, implying that rank

437 similarity in the patterns is accurately preserved during information processing.  
438 Furthermore, the pattern separation gain  $\gamma$  is highest ( $> 10$ ) for very similar patterns,  
439 demonstrating that small differences at the input level are amplified into large  
440 differences at the output level. These functional properties will be suitable to run  
441 similarity searches (termed locality-sensitive hashing in computer science)<sup>35</sup> or to  
442 perform similarity-based clustering of contextual input information<sup>63</sup>. Thus, the EC–DG–  
443 CA3 network may be computationally more powerful than previously thought.

444 Finally, our network model may help to develop new algorithms and  
445 computational architectures of technical deep learning networks<sup>51</sup>. Deep learning  
446 algorithms successfully incorporated the multi-layer structure of biological networks, the  
447 hippocampal network being the “prototype”. Although such technical networks are  
448 remarkably powerful, they lack the robustness, energy efficiency, and memory capability  
449 of biological networks. Incorporation of fast lateral inhibition and presynaptic short-term  
450 memory may increase the efficacy of such systems.

451 Full-size implementation is a strength of the present study. However, limitations  
452 were unavoidable. These include use of simplified cellular units (i.e. integrate-and-fire  
453 neurons for GCs, single-compartment neurons for INs), lack of less abundant cell types  
454 (such as somatostatin<sup>+</sup> or vasointestinal peptide<sup>+</sup> GABAergic interneurons, mossy cells,  
455 and newborn GCs)<sup>64,65</sup>, and simplified connectivity rules (e.g. for EC–GC perforant path  
456 connections where experimental connectivity data are currently unavailable). Increase  
457 in computational power of modeling hardware may allow us to address these limitations  
458 in the future.

459

460

461

## 462 **Methods**

### 463 **Topology of a full-size DG network model**

464 The pattern separation network model consists of three layers, the first layer  
465 representing the EC, with 50,000 ECs, the second layer representing the DG, with  
466 500,000 GCs and 2,500 PV<sup>+</sup>-INs, and the third layer representing the CA3 region, with  
467 250,000 pyramidal cells. First and second layer were connected by EC–GC synapses,  
468 representing the PP input to the DG. A winner-takes-all mechanism mediated by lateral  
469 inhibition was implemented by connecting GCs and INs by excitatory E–I synapses in  
470 one direction and by inhibitory I–E synapses in the other direction. Second and third  
471 layer were connected by GC–CA3 pyramidal neuron synapses, representing  
472 hippocampal mossy fiber synapses.

473 Unlike many network models, our model was implemented in full size  
474 (Supplementary Table 1). The number of GCs was chosen to represent the DG of one  
475 hemisphere of adult laboratory mice<sup>13</sup>. Full-scale implementation was necessary: (1) to  
476 increase the realism of the simulations, (2) to be able to implement measured  
477 macroscopic connectivity rules without scaling<sup>66</sup>, and (3) to simulate sparse coding  
478 regimes, which were unstable in smaller networks. The model was designed to  
479 incorporate the connectivity rules of PV<sup>+</sup>-INs and GCs in the DG (Supplementary Table  
480 1)<sup>22</sup>. Other types of INs were not implemented in the default model, because of their  
481 lower connectivity<sup>22</sup> and their slower signaling speed<sup>46</sup>. In total, the conclusions of the  
482 present paper were based on 784 full-scale simulations.

483

#### 484 **Implementation of inhibitory INs**

485 INs were implemented as single-compartment, conductance-based neurons endowed  
486 with modified Hodgkin-Huxley-type conductances<sup>67</sup> to capture the electrical properties  
487 of PV<sup>+</sup>-INs. Membrane potential was simulated by solving the equation:

$$488 \quad \frac{dV}{dt} = \frac{1}{C_m} (I_{drive} - I_{Na} - I_K - I_L), \quad (\text{Eq. 1})$$

489 where  $V$  is membrane potential,  $t$  is time,  $C_m$  is membrane capacitance,  $I_{drive}$  is driving  
490 current, and  $I_{Na}$ ,  $I_K$ , and  $I_L$  represent sodium, potassium and leakage current,  
491 respectively.  $I_{Na}$  was modeled as

492 
$$I_{Na} = \overline{g_{Na}} m^3 h (V - V_{Na}), \quad (\text{Eq. 2})$$

493 where  $\overline{g_{Na}}$  is the maximal sodium conductance,  $m$  is the activation parameter,  $h$  is the  
494 inactivation parameter, and  $V_{Na}$  represents the sodium ion equilibrium potential.

495 Similarly,  $I_K$  was modeled according to the equation

496 
$$I_K = \overline{g_K} n^4 (V - V_K), \quad (\text{Eq. 3})$$

497 where  $\overline{g_K}$  is the maximal potassium conductance,  $n$  is the activation parameter, and  $V_K$   
498 represents the potassium ion equilibrium potential.

499 Finally,  $I_L$  was given as

500 
$$I_L = g_L (V - V_L), \quad (\text{Eq. 4})$$

501 where  $g_L$  is leakage conductance and  $V_L$  is corresponding reversal potential.

502 State parameters  $m$ ,  $h$ , and  $n$  were computed according to the differential equation

503 
$$\frac{dm}{dt} = \alpha_m (1 - m) + \beta_m m \quad (\text{Eq. 5})$$

504 and equivalent equations for  $h$  and  $n$ .

505  $\alpha_m$ ,  $\alpha_h$ ,  $\alpha_n$  values and  $\beta_m$ ,  $\beta_h$ ,  $\beta_n$  values were calculated according to the equations  $\alpha_m =$   
506  $0.1 \text{ ms}^{-1} \times -(V+35 \text{ mV}) / \{\text{Exp}[-(V+35 \text{ mV})/10 \text{ mV}] - 1\}$ ,  $\beta_m = 4 \text{ ms}^{-1} \times$   
507  $\text{Exp}[-(V+60 \text{ mV})/18 \text{ mV}]$ ,  $\alpha_h = 0.35 \text{ ms}^{-1} \times \text{Exp}[-(V+58 \text{ mV})/20 \text{ mV}]$ ,  $\beta_h = 5 \text{ ms}^{-1} /$   
508  $\{\text{Exp}[-(V+28 \text{ mV})/10 \text{ mV}] + 1\}$ ,  $\alpha_n = 0.05 \text{ ms}^{-1} \times -(V+34 \text{ mV}) /$   
509  $\{\text{Exp}[-(V+34 \text{ mV})/10 \text{ mV}] - 1\}$ , and  $\beta_n = 0.625 \text{ ms}^{-1} \times \text{Exp}[-(V+44 \text{ mV})/80 \text{ mV}]^{67}$ . Single  
510 neurons were assumed to be cylinders with diameter and length of 70  $\mu\text{m}$ , giving a  
511 surface area of 15,394  $\mu\text{m}^2$  and an input resistance of 65  $\text{M}\Omega^{47}$ . Neurons showed a  
512 rheobase of 39 pA and a fast-spiking, type I AP phenotype<sup>68</sup>, as characteristic for PV<sup>+</sup>-  
513 INs<sup>46</sup>. Maximal conductance values were set as  $\overline{g_{Na}} = 35 \text{ mS cm}^{-2}$ ,  $\overline{g_K} = 9 \text{ mS cm}^{-2}$ ,  
514 and  $g_L = 0.1 \text{ mS cm}^{-2}$ ;  $V_{Na}$ ,  $V_K$ , and  $V_L$  were assumed as 55 mV, -90 mV, and -65 mV,  
515 respectively<sup>67</sup>.

516

## 517 **Implementation of GCs**

518 GCs were implemented as spiking neurons with leaky integrate-and-fire (LIF) firing  
519 properties, accelerating all computations by approximately an order of magnitude. To  
520 enable the integration of excitatory and inhibitory synaptic events with different kinetics,  
521 the standard LIF model was extended as follows<sup>69</sup>:

522 The time course of synaptic excitation was described by the differential equation

$$523 \quad \frac{de}{dt} = -k_e e, \quad (\text{Eq. 6})$$

524 where  $k_e$  is the synaptic excitation rate constant, i.e. the inverse of the time constant.

525 Likewise, the time course of synaptic inhibition was described by the differential  
526 equation

$$527 \quad \frac{di}{dt} = -k_i i, \quad (\text{Eq. 7})$$

528 where  $k_i$  is the synaptic inhibition rate constant.

529 Finally, the firing of the neuron was controlled by a membrane state variable  $v$ ;  
530 when  $v$  reaches 1, the cell fires, which resets the membrane by returning  $v$  to 0. The  
531 time course of  $v$  was determined by the differential equation

$$532 \quad \frac{dv}{dt} = -k_m v + a_e e + a_i i + i_{drive}, \quad (\text{Eq. 8})$$

533 where  $k_m$  is inverse of the membrane time constant,  $a_e$  and  $a_i$  are amplitudes of synaptic  
534 events, and  $i_{drive}$  represents the excitatory drive any given neuron receives<sup>69</sup>. Excitation  
535 time constant, inhibition time constant, and membrane time constant were set to 3, 10,  
536 and 15 ms, respectively (Supplementary Table 1)<sup>22,48,70</sup>. The refractory period was  
537 assumed as 5 ms.

538

## 539 **Implementation of synaptic interconnectivity**

540 Synapses between neurons were placed with distance-dependent probability.  
541 Normalized distance was cyclically measured as

542  $x = 0.5 - \text{abs}\{\text{abs}[(i / i_{\max} - j / j_{\max})] - 0.5\}$  , (Eq. 9)

543 where  $i$  and  $j$  are indices of pre- and postsynaptic neurons,  $i_{\max}$  and  $j_{\max}$  are  
 544 corresponding maximum index values, and  $\text{abs}(r)$  is the absolute value of a real number  
 545  $r$ . Connection probability was then computed with a Gaussian function as

546  $p(x) = c e^{-\frac{x^2}{2\sigma^2}}$  , (Eq. 10)

547 where  $c$  is maximal connection probability ( $c_{E-I}$ ,  $c_{I-E}$ ,  $c_{I-I}$ , and  $c_{\text{gap}}$ , respectively) and  $\sigma$  is  
 548 the standard deviation representing the width of the distribution ( $\sigma_{E-I}$ ,  $\sigma_{I-E}$ ,  $\sigma_{I-I}$ , and  $\sigma_{\text{gap}}$ ;  
 549 Supplementary Table 1).

550 The connection probability between ECs and GCs was computed from a  
 551 Gaussian function with peak connection probability of 0.2 and a standard deviation of  
 552 500  $\mu\text{m}$ , to represent the divergent connectivity from the EC to the DG<sup>27,32,45</sup>. Binary  
 553 activity patterns in upstream ECs were converted into patterns of excitatory drive of  
 554 GCs. Although this drive was primarily intended to represent input from EC neurons, it  
 555 may include contributions from other types of excitatory neurons<sup>64</sup>.

556 Excitatory GC–IN synapses, inhibitory IN–GC synapses, and inhibitory IN–IN  
 557 synapses were incorporated by random placement of NetCon objects in NEURON<sup>69</sup>;  
 558 gap junctions between PV<sup>+</sup>-INs were implemented by random placement of pairs of  
 559 point processes. For excitatory GC–IN synapses and inhibitory IN–IN synapses,  
 560 synaptic events were simulated using the Exp2Syn class of NEURON. For excitatory  
 561 GC–IN synapses, we assumed  $\tau_{\text{rise,E}} = 0.1$  ms,  $\tau_{\text{decay,E}} = 1$  ms, and a peak conductance  
 562 of 8 nS (Supplementary Table 1)<sup>21,22</sup>. For inhibitory IN–IN synapses, we chose  $\tau_{\text{rise,I}} =$   
 563 0.1 ms,  $\tau_{\text{decay,I}} = 2.5$  ms, and a peak conductance of 16 nS (Supplementary Table  
 564 1)<sup>22,37,59</sup>. For inhibitory IN–GC synapses, the synaptic weight was chosen as 0.025  
 565 (unitless, because GCs were modelled as LIF neurons). For all chemical synapses,  
 566 synaptic latency was between 0 and 25 ms, according to distance between pre- and  
 567 postsynaptic neuron. Gap junction resistance was assumed as 300 M $\Omega$ , approximately  
 568 five times the input resistance of a single cell (Supplementary Table 1)<sup>22,37,59</sup>. Synaptic  
 569 reversal potentials were 0 mV for excitation and –65 mV for inhibition. The maximal

570 length of the hippocampal network was assumed as 5 mm, consistent with anatomical  
571 descriptions in mice<sup>71</sup>.

572

### 573 **Detailed implementation and simulations**

574 Simulations of network activity were performed using NEURON version 7.6.2, 7.7.2, or  
575 7.8.2<sup>69</sup> in combination with Mathematica version 11.3.0.0 or 12.2.0.0 (Wolfram  
576 Research). Simulations were tested on a Lenovo T470p PC running under Windows 10.  
577 Final full-size simulations were run on the IST computer cluster under Debian  
578 GNU/Linux version 9 or 10 (<https://www.debian.org/>), the scheduling system slurm  
579 16.05, and the environment module system Lmod 7.7.

580 Simulations were performed in four steps (Supplementary Fig. 1). First, we  
581 computed random binary activity patterns in ECs. To generate input patterns with  
582 defined correlations over a wide range, 100 uncorrelated random vectors  $a_i$  of size  $n_{EC}$   
583 were computed, where individual elements are pseudorandom real numbers in range of  
584 0 to 1 and  $n_{EC}$  is the number of ECs. Uncorrelated vectors were transformed into  
585 correlated vectors as  $r \times a_1 + (1 - r) \times a_i$ , where  $a_1$  is the first random vector and  $r$  is a  
586 correlation factor.  $r$  was varied between 0.1 and 1. Finally, a threshold function  $f(x) =$   
587  $H(x - \theta)$  was applied to the vectors, where  $H$  is the Heaviside function and  $\theta$  is the  
588 threshold that determines the activity level in the pattern. Empirically, 100 input patterns  
589 were sufficient to continuously cover the chosen range of input correlations. Unless  
590 stated differently, the average activity in EC neurons ( $\alpha_{EC}$ ), i.e. the proportion of spiking  
591 cells, was assumed to be 0.1.

592 Second, the patterns in the upstream neurons were converted into patterns of  
593 excitatory drive in GCs, by multiplying the activity vectors with the previously computed  
594 connectivity matrix between EC neurons and GCs. Unless otherwise indicated, the  
595 mean tonic current value was set to 1.8 times the threshold value of the GCs (i.e.  $I_{\mu} =$   
596 1.8; unitless, since GCs were implemented as LIF units; Supplementary Table 1).

597 Third, we computed the activity of the network for all 100 patterns. Simulations  
 598 were run with 5  $\mu$ s fixed time step over a total duration of 50 or 60 ms. At the beginning  
 599 of each simulation, random number generators were initialized with defined seeds to  
 600 ensure reproducibility. At time 0, an inhibitory synaptic event of weight 1 (relative to  
 601 threshold) was simulated in all GCs to mimic recovery from gamma-modulated  
 602 inhibition<sup>19</sup>. Spikes were detected when membrane potential reached a value of 1 in the  
 603 GCs and 0 mV in the INs. Subsequently, spike times were displayed in raster plot  
 604 representations. Furthermore, 100 binary output vectors were computed, by setting the  
 605 value to 1 if a cell generated  $\geq 1$  spikes in the simulation time interval, and to 0  
 606 otherwise.

607 Finally, Pearson's correlation coefficients were calculated for all pairs of patterns  
 608 ( $\binom{100}{2} = 4,950$  points), at both input and output level in parallel as

$$609 \quad R = \frac{\text{Cov}(n_1, n_2)}{\sqrt{\text{Var}(n_1)\text{Var}(n_2)}}, \quad (\text{Eq. 11})$$

610 where Cov is covariance, Var is variance, and  $n_1$  and  $n_2$  are two given pattern  
 611 vectors. Because of mean value subtraction and normalization, this correlation measure  
 612 is per se independent of activity<sup>53</sup>. Next, output correlation coefficients ( $R_{\text{out}}$ ) were  
 613 plotted against input correlation coefficients ( $R_{\text{in}}$ ). For models activated by Poisson  
 614 trains of PP input (Supplementary Fig. 3) or implementing variation of synaptic  
 615 amplitude (Supplementary Fig. 7),  $R_{\text{out}}-R_{\text{in}}$  curves were normalized to the average  $R_{\text{out}}$   
 616 values obtained for identical patterns ( $R_{\text{in}} = 1$ ), which were  $< 1$  because of the stochastic  
 617 nature of the models. For models with heterogeneity of excitability (Supplementary Fig.  
 618 8),  $R_{\text{out}}-R_{\text{in}}$  curves were normalized to the average  $R_{\text{out}}$  values obtained for uncorrelated  
 619 patterns ( $R_{\text{in}} \rightarrow 0$ ), which were  $> 0$  because the cells with the highest excitability were  
 620 consistently firing, whereas the cells with the lowest excitability were consistently silent.  
 621 Pattern separation was quantitatively characterized by three parameters: (1) The  
 622 efficacy of pattern separation ( $\psi$ ) was quantified by an integral-based index, defined as  
 623 the area between the identity line and the  $R_{\text{out}}$  versus  $R_{\text{in}}$  curve, normalized by the area  
 624 under the identity line ( $\frac{1}{2}$ ). Thus,

625  $\psi = 2 \int_{x=0}^1 (x - f(x)) dx$  , (Eq. 12)

626 where  $f(x)$  represents the input-output correlation function. In practice, data points were  
 627 sorted by  $R_{in}$  values, and points with same  $R_{in}$  were averaged.  $f(x)$  was determined as a  
 628 5<sup>th</sup> or 10<sup>th</sup>-order polynomial function  $f(x)$  fit to the  $R_{out}$  versus  $R_{in}$  data points;  $f(x)$  was  
 629 constrained to pass through points (0|0) and (1|1). Based on the definition of Eq. 12, a  $\psi$   
 630 value close to 1 would correspond to an ideal pattern separator. In contrast,  $\psi = 0$  would  
 631 represent pattern identity, whereas  $\psi < 0$  would indicate pattern completion. (2) The  
 632 gain of pattern separation ( $\gamma$ ) was quantified from the maximal slope of the  $R_{out}$  versus  
 633  $R_{in}$  curve. In practice, this value was determined from the first derivative of the  
 634 polynomial function  $f(x)$  fit to the  $R_{out}$  versus  $R_{in}$  data points as  $\lim_{x \rightarrow 1} \left( \frac{df(x)}{dx} \right)$ . A  $\gamma$  value  
 635  $\gg 1$  would correspond to an ideal pattern separator. In contrast,  $\gamma = 1$  would represent  
 636 pattern identity, whereas  $\gamma < 1$  may indicate pattern completion. (3) The reliability of  
 637 pattern separation ( $\rho$ ) was quantified by the Pearson's correlation coefficient of the  
 638 ranks of all  $R_{out}$  versus the ranks of the corresponding  $R_{in}$  data points. An ideal pattern  
 639 separator will maintain the order of pairwise correlations: if a pair of patterns is more  
 640 similar than another pair at the input level, it will be also more similar at the output level.  
 641 Thus, for an ideal pattern separator,  $\rho$  will be close to 1 (Refs. 34–36).

642 To analyze the effects of convergence and divergence on pattern separation  
 643 (Fig. 3a–d), activity was simulated in ECs, converted into drive patterns in GCs by  
 644 multiplication with the EC–GC connectivity matrix, and finally converted into binary  
 645 activity values in GCs by applying a threshold corresponding to the desired activity level  
 646  $\alpha$ . This simplified approach permitted systematic variation of model parameters (e.g. cell  
 647 numbers and connection probabilities) over a wide range. In the simulations, both  $n_{EC}$   
 648 and  $n_{GC}$  was varied between 10,000 and 100,000, yielding ratios ranging from 1 : 10 to  
 649 10 : 1. Unless specified differently, in these simplified simulations activity in the EC ( $\alpha_{EC}$ )  
 650 was set to 0.1, and EC–GC connectivity was assumed to be random with an average  
 651 connection probability ( $C_{EC-GC}$ ) of 0.05

652 To address the effects of plasticity at PP synapses on pattern computations (Fig.  
653 6a–c), we introduced an associative synaptic plasticity rule at EC–GC synapses. We  
654 first simulated the responses of the network to 100 EC patterns with the default  
655 parameter set in a control run. Coincident pre- and postsynaptic activity was  
656 cumulatively recorded for all synapses across all patterns. Next, we computed the  
657 extent of potentiation for each EC–GC synapse according to a sigmoidal function of the  
658 form

$$659 \quad f(x) = f_{\text{pot}} / (1 + \exp[-(x - x_{\text{half}}) / k]), \quad (\text{Eq. 13})$$

660 where  $f_{\text{pot}}$  is the potentiation,  $x$  is the number of coincident APs,  $x_{\text{half}}$  is the number of  
661 APs leading to half-maximal potentiation, and  $k$  is a slope factor. As default values,  $x_{\text{half}}$   
662 = 5 and  $k = 5$  were used. Finally, we simulated the responses of the network to 100 EC  
663 patterns with the potentiated synapses in a test run (Fig. 6a–c).

664

### 665 **Robustness of the pattern separation mechanism**

666 Unless specified differently, standard parameter values (Supplementary Table 1) were  
667 used for all simulations. However, several additional simulations were performed to test  
668 the robustness of pattern separation against parameter variation. (1) To test the effects  
669 of conductance-based synapses against current-based synapses (Supplementary Fig.  
670 2), GCs were simulated as single-compartment conductance-based neurons with  
671 passive properties. (2) To test the effects of temporal structure of the excitatory drive  
672 (Supplementary Fig. 3), the tonic current was replaced by Poisson trains of excitatory  
673 postsynaptic currents (EPSCs). In these simulations, events were simulated by NetStim  
674 processes. (3) To generate spatially correlated patterns (Supplementary Fig. 4), random  
675 numbers were drawn from a multinormal distribution with exponential spatial correlation  
676 (length constant 15,000 cells) and thresholded to give a spatially correlated binary  
677 pattern with appropriate activity level. (4) To implement feedforward inhibition  
678 (Supplementary Fig. 5), the tonic excitatory drive computed from EC activity and EC–  
679 GC connectivity was applied in parallel to INs after appropriate scaling. (5) To replace  
680 PV<sup>+</sup>-INs with CCK<sup>+</sup>-like IN subtypes (e.g. hilar INs with axons associated with the

681 commissural / associational pathway; Supplementary Fig. 6a)<sup>72-75</sup>, model parameters  
682 were changed to account for reduced connectivity, altered synaptic strength, and slower  
683 signaling according to the replacement rules  $c_{E-I} = 0.1 \rightarrow 0.02$ ,  $g_{I-E} = 0.3 \rightarrow 0.1$ ,  $J_{E-I} =$   
684  $0.008 \rightarrow 0.004$  nS,  $J_{I-E} = 0.025 \rightarrow 0.05$ ,  $\tau_{I-E} = 10 \rightarrow 20$  ms, and  $\tau_m = 10 \rightarrow 20$  ms. In  
685 addition, to incorporate CCK<sup>+</sup>-like IN subtypes in the network (Supplementary Fig. 6b),  
686 an increasing number of neurons with the following connectivity parameters were added  
687 to the model:  $c_{CCK-CCK} = 0.2$ ,  $c_{PV-CCK} = 0.6$ ,  $c_{CCK-PV} = 0.2$ ,  $c_{E-CCK} = 0.02$ ,  $c_{CCK-E} = 0.1$ ,  $J_{E-}$   
688  $CCK = 4$  nS,  $J_{CCK-E} = 0.05$ ,  $J_{CCK-CCK} = 16$  nS,  $J_{PV-CCK} = 16$  nS, and  $J_{CCK-PV} = 16$  nS. (6)  
689 To incorporate PP inputs to CA3 pyramidal neurons (Fig. 6d-f)<sup>32</sup>, the tonic excitatory  
690 drive computed from EC activity and EC-GC connectivity was applied in parallel to CA3  
691 pyramidal neurons. (7) To test the effects of synaptic heterogeneity (Supplementary Fig.  
692 7), synaptic amplitudes at all synapses were drawn from normal distributions with  
693 specified coefficient of variation, CV. Both trial-to-trial (“type 1”) and synapse-to-synapse  
694 (“type 2”) variability were examined. (8) Finally, to test the effects of heterogeneity in GC  
695 excitability (Supplementary Fig. 8), the constant firing threshold (by default 1 in LIF  
696 neurons) was replaced by random threshold values for individual cells drawn from a  
697 normal distribution with mean 1 and standard deviation  $\sigma_{thres}$ .

698

## 699 Conventions

700 Throughout the paper, model parameters given in Supplementary Table 1 are referred  
701 to as standard parameters. In summary bar graphs, black bars indicate these standard  
702 values, light blue bars reduced values, and light red bars increased values in  
703 comparison to the default parameter set. In functional analysis of  $\psi$ ,  $\gamma$ , and  $\rho$ , standard  
704 parameters are indicated as vertical dashed. Throughout the paper, the term “pattern” is  
705 defined as a vector of real values (for excitatory drive) or a vector of binary values (for  
706 activity, 1 if the cell fires, 0 otherwise). In both cases, the vector length corresponds to  
707 the number of cells.

708

## 709 Data availability

710 Source Data for Figures 1–6 and Extended Data Figure 1 are provided with this  
711 manuscript. Output data sets can be regenerated from the code<sup>76</sup>. As the full output  
712 dataset generated in this work is huge (> 10 Terabyte), deposit in a publicly available  
713 repository is not practical at the current time point. Specific data will be provided by the  
714 corresponding author upon request (Peter.Jonas@ist.ac.at).

715

## 716 **Code availability**

717 A minimal version of the Neuron simulation code is provided as Supplementary  
718 Software. A full version of the simulation and analysis code has been deposited in a  
719 publicly available DOI-minting repository under the GNU General Public License version  
720 3, as published by the Free Software Foundation (Ref. 76).

721

## 722 **References**

- 723 1. Yassa, M.A., & Stark, C.E. Pattern separation in the hippocampus. *Trends in*  
724 *Neurosciences* **34**, 515–525 (2011).
- 725 2. Rolls, E.T. Pattern separation, completion, and categorisation in the  
726 hippocampus and neocortex. *Neurobiology of Learning and Memory* **129**, 4–28  
727 (2016).
- 728 3. Chavlis, S., & Poirazi, P. Pattern separation in the hippocampus through the eyes  
729 of computational modeling. *Synapse* **71**, e21972 (2017).
- 730 4. Cayco-Gajic, N.A., & Silver, R.A. Re-evaluating circuit mechanisms underlying  
731 pattern separation. *Neuron* **101**, 584–602 (2019).
- 732 5. Leutgeb, J.K., Leutgeb, S., Moser, M.B., & Moser, E.I. Pattern separation in the  
733 dentate gyrus and CA3 of the hippocampus. *Science* **315**, 961–966 (2007).
- 734 6. Scharfman, H.E. The dentate gyrus: A comprehensive guide to structure,  
735 function, and clinical implications. *Progress in Brain Research* **163**, 627–637  
736 (2007).

- 737 7. Bischofberger, J., Engel, D., Frotscher, M., & Jonas, P. Timing and efficacy of  
738 transmitter release at mossy fiber synapses in the hippocampal network. *Pflügers*  
739 *Archiv* **453**, 361–372 (2006).
- 740 8. Guzman, S.J., Schlögl, A., Frotscher, M., & Jonas, P. Synaptic mechanisms of  
741 pattern completion in the hippocampal CA3 network. *Science* **353**, 1117–1123  
742 (2016).
- 743 9. Marr, D. A theory of cerebellar cortex. *Journal of Physiology* **202**, 437–470  
744 (1969).
- 745 10. Albus, J.S. A Theory of Cerebellar Function. *Mathematical Biosciences* **10**, 25–  
746 61 (1971).
- 747 11. Amaral, D.G., Ishizuka, N., & Claiborne, B. Neurons, numbers and the  
748 hippocampal network. *Progress in Brain Research* **83**, 1–11 (1990).
- 749 12. Boss, B.D., Turlejski, K., Stanfield, B.B., & Cowan, W.M. On the numbers of  
750 neurons in fields CA1 and CA3 of the hippocampus of Sprague-Dawley and  
751 Wistar rats. *Brain Research* **406**, 280–287 (1987).
- 752 13. Amrein, I., Slomianka, L., & Lipp, H.P. Granule cell number, cell death and cell  
753 proliferation in the dentate gyrus of wild-living rodents. *European Journal of*  
754 *Neuroscience* **20**, 3342–3350 (2004).
- 755 14. Coultrip, R., Granger, R., & Lynch, G. A cortical model of winner-take-all  
756 competition via lateral inhibition. *Neural Networks* **5**, 47–54 (1992).
- 757 15. Wiechert, M.T., Judkewitz, B., Riecke, H., & Friedrich, R.W. Mechanisms of  
758 pattern decorrelation by recurrent neuronal circuits. *Nature Neuroscience* **13**,  
759 1003–1010 (2010).
- 760 16. Papadopoulou, M., Cassenaer, S., Nowotny, T., & Laurent, G. Normalization for  
761 sparse encoding of odors by a wide-field interneuron. *Science* **332**, 721–725  
762 (2011).
- 763 17. Lin, A.C., Bygrave, A.M., de Calignon, A., Lee, T., & Miesenböck, G. Sparse,  
764 decorrelated odor coding in the mushroom body enhances learned odor  
765 discrimination. *Nature Neuroscience* **17**, 559–568 (2014).
- 766 18. Maass, W. On the computational power of winner-take-all. *Neural Computation*  
767 **12**, 2519–2535 (2000).

- 768 19. de Almeida, L., Idiart, M., & Lisman, J.E. A second function of gamma frequency  
769 oscillations: an  $E\%$ -max winner-take-all mechanism selects which cells fire.  
770 *Journal of Neuroscience* **29**, 7497–7503 (2009).
- 771 20. Tetzlaff, T., Helias, M., Einevoll, G.T., & Diesmann, M. Decorrelation of neural-  
772 network activity by inhibitory feedback. *PLoS Computational Biology* **8**, e1002596  
773 (2012).
- 774 21. Geiger, J.R.P., Lübke, J., Roth, A., Frotscher, M., & Jonas, P. Submillisecond  
775 AMPA receptor-mediated signaling at a principal neuron-interneuron synapse.  
776 *Neuron* **18**, 1009–1023 (1997).
- 777 22. Espinoza, C., Guzman, S.J., Zhang, X., & Jonas, P. Parvalbumin<sup>+</sup> interneurons  
778 obey unique connectivity rules and establish a powerful lateral-inhibition  
779 microcircuit in dentate gyrus. *Nature Communications* **9**, 4605 (2018).
- 780 23. O'Reilly, R.C., & McClelland, J.L. Hippocampal conjunctive encoding, storage,  
781 and recall: avoiding a trade-off. *Hippocampus* **4**, 661–682 (1994).
- 782 24. Neunuebel, J.P., & Knierim, J.J. CA3 retrieves coherent representations from  
783 degraded input: direct evidence for CA3 pattern completion and dentate gyrus  
784 pattern separation. *Neuron* **81**, 416–427 (2014).
- 785 25. Vyleta, N.P., Borges-Merjane, C., & Jonas, P. Plasticity-dependent, full  
786 detonation at hippocampal mossy fiber-CA3 pyramidal neuron synapses. *Elife* **5**,  
787 e17977 (2016).
- 788 26. Cayco-Gajic, N.A., Clopath, C., & Silver, R.A. Sparse synaptic connectivity is  
789 required for decorrelation and pattern separation in feedforward networks. *Nature*  
790 *Communications* **8**, 1116 (2017).
- 791 27. Witter, M.P. The perforant path: projections from the entorhinal cortex to the  
792 dentate gyrus. *Progress in Brain Research* **163**, 43–61 (2007).
- 793 28. Bliss, T.V.P., & Lømo, T. Long-lasting potentiation of synaptic transmission in the  
794 dentate area of the anaesthetized rabbit following stimulation of the perforant  
795 path. *Journal of Physiology* **232**, 331–356 (1973).

- 796 29. McNaughton, B.L., Douglas, R.M., & Goddard, G.V. Synaptic enhancement in  
797 fascia dentata: cooperativity among coactive afferents. *Brain Research* **157**,  
798 277–293 (1978).
- 799 30. McHugh, T.J., Jones, M.W., Quinn, J.J., Balthasar, N., Coppari, R., Elmquist,  
800 J.K., Lowell, B.B., Fanselow, M.S., Wilson, M.A., & Tonegawa, S. Dentate gyrus  
801 NMDA receptors mediate rapid pattern separation in the hippocampal network.  
802 *Science* **317**, 94–99 (2007).
- 803 31. McNaughton, B.L., & Morris, R.G.M. Hippocampal synaptic enhancement and  
804 information storage within a distributed memory system. *Trends Neuroscience*  
805 **10**, 408–415 (1987).
- 806 32. Steward, O. Topographic organization of the projections from the entorhinal area  
807 to the hippocampal formation of the rat. *Journal of Comparative Neurology* **167**,  
808 285–314 (1976).
- 809 33. Zhang, X., Schlögl, A., & Jonas, P. Selective routing of spatial information flow  
810 from input to output in hippocampal granule cells. *Neuron* **107**, 1212–1225  
811 (2020).
- 812 34. Valiant, L.G. The hippocampus as a stable memory allocator for cortex. *Neural*  
813 *Computation* **24**, 2873–2899 (2012).
- 814 35. Dasgupta, S., Stevens, C.F., & Navlakha, S. A neural algorithm for a  
815 fundamental computing problem. *Science* **358**, 793–796 (2017).
- 816 36. Sharma J., & Navlakha, S. Improving similarity search with high-dimensional  
817 locality-sensitive hashing. arXiv:1812.01844v1 (2018).
- 818 37. Bartos, M., Vida, I., Frotscher, M., Meyer, A., Monyer, H., Geiger, J.R.P., &  
819 Jonas, P. Fast synaptic inhibition promotes synchronized gamma oscillations in  
820 hippocampal interneuron networks. *Proceedings of the National Academy of*  
821 *Sciences of the United States of America* **99**, 13222–13227 (2002).
- 822 38. Claiborne, B.J., Amaral, D.G., & Cowan, W.M. A light and electron microscopic  
823 analysis of the mossy fibers of the rat dentate gyrus. *Journal of Comparative*  
824 *Neurology* **246**, 435–458 (1986).

- 825 39. Henze, D.A., Wittner, L., & Buzsáki, G. Single granule cells reliably discharge  
826 targets in the hippocampal CA3 network *in vivo*. *Nature Neuroscience* **5**, 790–  
827 795 (2002).
- 828 40. Vandael, D., Borges-Merjane, C., Zhang, X., & Jonas, P. Short-term plasticity at  
829 hippocampal mossy fiber synapses is induced by natural activity patterns and  
830 associated with vesicle pool engram formation. *Neuron* **107**, 509–521 (2020).
- 831 41. Bragin, A., Jandó, G., Nádasdy, Z., Hetke, J., Wise, K., & Buzsáki, G. Gamma  
832 (40–100 Hz) oscillation in the hippocampus of the behaving rat. *Journal of*  
833 *Neuroscience* **15**, 47–60 (1995).
- 834 42. Pernía-Andrade, A.J., & Jonas, P. Theta-gamma-modulated synaptic currents in  
835 hippocampal granule cells *in vivo* define a mechanism for network oscillations.  
836 *Neuron* **81**, 140–152 (2014).
- 837 43. Majani, E., Erlanson, R., & Abu-Mostafa, Y. On the k-winners takes-all network.  
838 *Advances in Neural Information Processing Systems* **1**, 634–642 (1989).
- 839 44. Ellias, S.A., & Grossberg, S. Pattern formation, contrast control, and oscillations  
840 in the short term memory of shunting on-center off-surround networks. *Biological*  
841 *Cybernetics* **20**, 69–98 (1975).
- 842 45. Tamamaki, N., & Nojyo, Y. Projection of the entorhinal layer II neurons in the rat  
843 as revealed by intracellular pressure-injection of neurobiotin. *Hippocampus* **3**,  
844 471–480 (1993).
- 845 46. Hu, H., Gan, J., & Jonas, P. Fast-spiking, parvalbumin<sup>+</sup> GABAergic interneurons:  
846 from cellular design to microcircuit function. *Science* **345**, 1255263 (2014).
- 847 47. Nörenberg, A., Hu, H., Vida, I., Bartos, M., & Jonas, P. Distinct nonuniform cable  
848 properties optimize rapid and efficient activation of fast-spiking GABAergic  
849 interneurons. *Proceedings of the National Academy of Sciences of the United*  
850 *States of America* **107**, 894–899 (2010).
- 851 48. Kraushaar, U., & Jonas, P. Efficacy and stability of quantal GABA release at a  
852 hippocampal interneuron-principal neuron synapse. *Journal of Neuroscience* **20**,  
853 5594–5607 (2000).

- 854 49. Chamberland, S., Timofeeva, Y., Evstratova, A., Volynski, K., & Tóth, K. Action  
855 potential counting at giant mossy fiber terminals gates information transfer in the  
856 hippocampus. *Proceedings of the National Academy of Sciences of the United*  
857 *States of America* **115**, 7434–7439 (2018).
- 858 50. Toth, K., Soares, G., Lawrence, J.J., Philips-Tansey, E., & McBain, C.J.  
859 Differential mechanisms of transmission at three types of mossy fiber synapse.  
860 *Journal of Neuroscience* **20**, 8279–8289 (2000).
- 861 51. LeCun, Y., Bengio, Y., & Hinton, G. Deep learning. *Nature* **521**, 436–444 (2015).
- 862 52. Babadi, B., & Sompolinsky, H. Sparseness and expansion in sensory  
863 representations. *Neuron* **83**, 1213–1226 (2014).
- 864 53. de la Rocha, J., Doiron, B., Shea-Brown, E., Josić, K., & Reyes, A. Correlation  
865 between neural spike trains increases with firing rate. *Nature* **448**, 802–806  
866 (2007).
- 867 54. Hoeffding, W. Masstabinvariante Korrelationsstheorie. *Schriften des*  
868 *Mathematischen Instituts und des Instituts für Angewandte Mathematik der*  
869 *Universität Berlin* **5**, 179–233 (1940).
- 870 55. Kowalski, J., Gan, J., Jonas, P., & Pernía-Andrade, A.J. Intrinsic membrane  
871 properties determine hippocampal differential firing pattern in vivo in anesthetized  
872 rats. *Hippocampus* **26**, 668–682 (2016).
- 873 56. Engin, E., Zarnowska, E.D., Benke, D., Tsvetkov, E., Sigal, M., Keist, R.,  
874 Bolshakov, V.Y., Pearce, R.A., & Rudolph, U. Tonic inhibitory control of dentate  
875 gyrus granule cells by  $\alpha 5$ -containing GABA<sub>A</sub> receptors reduces memory  
876 interference. *Journal of Neuroscience* **35**, 13698–13712 (2015).
- 877 57. Espinoza Martinez, C.M. Parvalbumin+ interneurons enable efficient pattern  
878 separation in hippocampal microcircuits. IST Austria, DOI:  
879 10.15479/AT:ISTA:6363 (2019).
- 880 58. Braganza, O., Mueller-Komorowska, D., Kelly, T., & Beck, H. Quantitative  
881 properties of a feedback circuit predict frequency-dependent pattern separation.  
882 *Elife* **9**, e53148 (2020).

- 883 59. Bartos, M., Vida, I., Frotscher, M., Geiger, J.R.P. & Jonas, P. Rapid signaling at  
884 inhibitory synapses in a dentate gyrus interneuron network. *Journal of*  
885 *Neuroscience* **21**, 2687–2698 (2001).
- 886 60. Hu, H., & Jonas, P. A supercritical density of Na<sup>+</sup> channels ensures fast signaling  
887 in GABAergic interneuron axons. *Nature Neuroscience* **17**, 686–693 (2014).
- 888 61. Bucurenciu, I., Kulik, A., Schwaller, B., Frotscher, M., & Jonas, P. Nanodomain  
889 coupling between Ca<sup>2+</sup> channels and Ca<sup>2+</sup> sensors promotes fast and efficient  
890 transmitter release at a cortical GABAergic synapse. *Neuron* **57**, 536–545  
891 (2008).
- 892 62. Jones, B.W., Deem, J., Younts, T.J., Weisenhaus, M., Sanford, C.A., Slack,  
893 M.C., Chin, J., Nachmanson, D., McKennon, A., Castillo, P.E., & McKnight, G.S.  
894 Targeted deletion of AKAP7 in dentate granule cells impairs spatial  
895 discrimination. *Elife* **5**, e20695 (2016).
- 896 63. Pehlevan, C., Sengupta, A.M., & Chklovskii, D.B. Why do similarity matching  
897 objectives lead to Hebbian/Anti-Hebbian networks? *Neural Computation* **30**, 84–  
898 124 (2018).
- 899 64. Myers, C.E., & Scharfman, H.E. A role for hilar cells in pattern separation in the  
900 dentate gyrus: a computational approach. *Hippocampus* **19**, 321–337 (2009).
- 901 65. Johnston, S.T., Shtrahman, M., Parylak, S., Gonçalves, J.T., & Gage, F.H.  
902 Paradox of pattern separation and adult neurogenesis: A dual role for new  
903 neurons balancing memory resolution and robustness. *Neurobiology of Learning*  
904 *and Memory* **129**, 60–68 (2016).
- 905 66. Schneider, C.J., Bezaire, M., & Soltesz, I. Toward a full-scale computational  
906 model of the rat dentate gyrus. *Frontiers in Neural Circuits* **6**, 83 (2012).
- 907 67. Wang, X.J., & Buzsáki, G. Gamma oscillation by synaptic inhibition in a  
908 hippocampal interneuronal network model. *Journal of Neuroscience* **16**, 6402–  
909 6413 (1996).
- 910 68. Ermentrout, B. Type I membranes, phase resetting curves, and synchrony.  
911 *Neural Computation* **8**, 979–1001 (1996).
- 912 69. Carnevale, N.T., & Hines, M.L. The Neuron book. *Cambridge University Press*  
913 (2006).

- 914 70. Schmidt-Hieber, C., Jonas, P., & Bischofberger, J. Subthreshold dendritic signal  
915 processing and coincidence detection in dentate gyrus granule cells. *Journal of*  
916 *Neuroscience* **27**, 8430–8441 (2007).
- 917 71. Paxinos, G., & Franklin, K. The mouse brain in stereotaxic coordinates.  
918 *Academic Press, Cambridge, MA*, 4th Edition (2012).
- 919 72. Han, Z.S., Buhl, E.H., Lörinczi, Z., & Somogyi, P. A high degree of spatial  
920 selectivity in the axonal and dendritic domains of physiologically identified local-  
921 circuit neurons in the dentate gyrus of the rat hippocampus. *European Journal of*  
922 *Neuroscience* **5**, 395–410 (1993).
- 923 73. Hefft, S., & Jonas, P. Asynchronous GABA release generates long-lasting  
924 inhibition at a hippocampal interneuron-principal neuron synapse. *Nature*  
925 *Neuroscience* **8**, 1319–1328 (2005).
- 926 74. Hosp, J.A., Strüber, M., Yanagawa, Y., Obata, K., Vida, I., Jonas, P., & Bartos,  
927 M. Morpho-physiological criteria divide dentate gyrus interneurons into classes.  
928 *Hippocampus* **24**, 189–203 (2014).
- 929 75. Armstrong, C., & Soltesz, I. Basket cell dichotomy in microcircuit function. *Journal*  
930 *of Physiology* **590**, 683–694 (2012).
- 931 76. Guzman, S.J. Schlögl, A., Espinoza, C., Zhang, X., Suter, B.A. & Jonas, P.  
932 Pattern separation network. DOI <https://doi.org/10.15479/AT:ISTA:10110> (2021).

933

## 934 **Acknowledgments**

935 We thank Drs. Ad Aertsen, Nancy Kopell, Wolfgang Maass, Arnd Roth, Federico Stella,  
936 and Tim Vogels for critically reading earlier versions of the manuscript. We are grateful  
937 to Florian Marr and Christina Altmutter for excellent technical assistance, Eleftheria  
938 Kralli-Beller for manuscript editing, and the Scientific Service Units of IST Austria for  
939 efficient support. Finally, we thank Drs. Ted Carnevale, Laszlo Erdős, Michael Hines,  
940 Duane Nykamp, and Dominik Schröder for useful discussions, and Rainer Friedrich and  
941 Simon Wiechert for sharing unpublished data. This project received funding from the  
942 European Research Council (ERC) under the European Union’s Horizon 2020 research

943 and innovation programme (grant agreement No 692692, P.J.) and the Fond zur  
944 Förderung der Wissenschaftlichen Forschung (Z 312-B27, Wittgenstein award to P.J.  
945 and P 31815 to S.J.G.).

946

#### 947 **Author contributions**

948 P.J. and S.J.G. designed the model and the layout of the simulations, P.J. and A.S.  
949 performed large-scale simulations on computer clusters, C.E., X.Z., and B.A.S. provided  
950 experimental data, P.J. and S.J.G. analyzed data, and P.J. wrote the paper. All authors  
951 jointly revised the paper.

952

#### 953 **Competing interest**

954 The authors declare no conflict of interest.

955

956

957 **Figure legends**

958 **Figure 1** | Pattern separation in a biologically realistic full-scale network model.

959 **a**, Structure of the biologically inspired full-scale model based on experimental data on  
960 synaptic connectivity and biophysical properties of cells and synapses. EC neurons,  
961 entorhinal cortex neurons; GCs, DG granule cells, PV<sup>+</sup>-INs, parvalbumin-expressing  
962 interneurons; CA3, CA3 pyramidal neurons. GCs and CA3 neurons were implemented  
963 as LIF neurons. PV<sup>+</sup>-INs were represented as single-compartment conductance-based  
964 models endowed with modified Hodgkin-Huxley-type conductances<sup>67</sup> to convey maximal  
965 realism to the pattern separation mechanism. GCs were activated by a tonic excitatory  
966 drive ( $I_{\mu}$ ), and an external inhibitory conductance was simulated to mimic gamma  
967 oscillations ( $J_{\text{gamma}}$ ). Cell numbers (right) were chosen to represent the hippocampus of  
968 one hemisphere in rodents<sup>13</sup>.

969 **b**, Activity in the pattern separation network model. Top, membrane potential in GCs  
970 (left, black), INs (center, red), and CA3 pyramidal neurons (right, gray). Traces from  
971 every 10<sup>th</sup> IN (250 traces total) and every 1,000<sup>th</sup> GC or CA3 pyramidal cell (500 and  
972 250 traces total, respectively) were superimposed. For GCs and CA3 pyramidal cells,  
973 membrane potential is unitless, since cells were simulated as LIF neurons. Bottom,  
974 rasterplots of AP generation in GCs (left, black), INs (center, red), and CA3 pyramidal  
975 neurons (right, gray). Each point indicates an AP.  $t = 0$  corresponds to onset of  
976 inhibitory conductance representing a gamma oscillation cycle in the network<sup>19</sup>.

977 **c–e**, Input–output correlation ( $R_{\text{out}}-R_{\text{in}}$ ) graphs at different levels of the network  
978 (standard parameter settings). Data points represent pairwise correlation coefficients  
979 between input patterns ( $R_{\text{in}}$ ) and corresponding output patterns ( $R_{\text{out}}$ ). Input-output  
980 correlation at first layer, measured between EC neurons and GCs (c), at second layer,  
981 measured between GCs and CA3 neurons (d), and across the entire network,  
982 measured between EC and CA3 neurons (e). Red dashed line, identity line; gray  
983 shaded area, area between data points and identity line, used for computation of  
984 integral-based pattern separation index,  $\psi$ . Blue line and light blue shaded area, tangent  
985 line at  $R_{\text{in}} = 1$  and corresponding slope triangle of a polynomial function fit to the data

986 points, used for computation of slope-based pattern separation index,  $\gamma$ . Insets,  
987 horizontally expanded view of tangent and slope triangle used to compute  $\gamma$ .

988 **f–h**, Preservation of rank order similarity between patterns at input and output. The  
989 rank-based pattern separation index,  $\rho$ , was computed as the correlation coefficient of  
990 ranked  $R_{out}$  versus ranked  $R_{in}$  data. Rank analysis at first layer, measured between EC  
991 and DG (f), at second layer, measured between DG and CA3 (g), and across the entire  
992 network, measured between EC and CA3 (h).

993

994

995 **Figure 2** | Dependence of pattern separation on gamma rhythm and lateral inhibition.

996 **a**, Analysis of effects of inhibition on pattern separation in a biologically inspired full-  
997 scale model of the DG. Lateral inhibition was mediated by PV<sup>+</sup>-INs included in the  
998 models. Gamma-modulated inhibition was included as synchronized external inhibitory  
999 conductance.

1000 **b**, Plot of  $\psi$  (red),  $\gamma$  (blue),  $\rho$  (green), and average activity  $\alpha$  (magenta) against  
1001 excitatory drive in GCs ( $I_{\mu}$ ), relative to threshold. Top left, default model, with both  
1002 gamma inhibition and lateral inhibition intact ( $J_{gamma} = 1$  relative to threshold,  $J_{E-I} = 8$  nS,  
1003  $J_{I-E} = 0.025$ , relative to threshold). Top right, gamma inhibition deleted ( $J_{gamma} = 0$ ).  
1004 Bottom left, lateral inhibition removed ( $J_{E-I} = 0$ ,  $J_{I-E} = 0$ ). Bottom right, both gamma  
1005 inhibition and lateral inhibition cancelled from the default model ( $J_{gamma} = 0$ ,  $J_{E-I} = 0$ ,  $J_{I-E}$   
1006  $= 0$ ). LI, lateral inhibition.

1007 **c**, Contour plot of  $\psi$  against the mean excitatory drive ( $I_{\mu}$ , abscissa) and amplitude of  
1008 gamma inhibition ( $J_{gamma}$ , ordinate). Contour lines indicate  $\psi$ ; warm colors represent  
1009 high values, cold colors indicate low values.

1010 **d**, Similar contour plot as shown in (c), but after removal of lateral inhibition. Analysis of  
1011 pattern separation was restricted to the region of the  $I_{\mu}$ - $J_{gamma}$  parameter space in  
1012 which activity  $\alpha$  was  $< 0.5$  (otherwise white).

1013 **e–g**, Interfering with lateral inhibition in different ways similarly affects pattern  
1014 separation. Top,  $\psi$  for different values of peak connection probability of excitatory E–I  
1015 connectivity ( $c_{E-I}$ , e), width of excitatory E–I connectivity ( $\sigma_{E-I}$ , f), and synaptic strength  
1016 of excitatory E–I synapses ( $J_{E-I}$ , g). Bottom, similar analysis, but for inhibitory I–E  
1017 connectivity ( $c_{I-E}$ , e;  $\sigma_{I-E}$ , f;  $J_{I-E}$ , g). Increasing  $c_{I-E}$ ,  $\sigma_{E-I}$  or  $\sigma_{I-E}$ , and  $J_{I-E}$  increased  
1018 pattern separation efficacy only minimally, whereas increasing  $c_{E-I}$  and  $J_{E-I}$  led to much  
1019 larger improvement. Thus,  $c_{I-E}$ ,  $\sigma_{E-I}$  or  $\sigma_{I-E}$ , and  $J_{I-E}$  appear to be near the optimum that  
1020 provides maximal pattern separation, whereas  $c_{E-I}$  and  $J_{E-I}$  are below the optimum.

1021

1022

1023 **Figure 3** | Independence of pattern separation on divergent excitatory connectivity  
1024 between EC neurons and GCs.

1025 **a**, Analysis of divergence and convergence in a simplified connectivity–thresholding  
1026 network. Binary activity vectors of the presynaptic layer were multiplied by a connectivity  
1027 matrix, resulting in drive vectors in the postsynaptic layer. Drive vectors were then  
1028 converted into binary vectors by thresholding. The threshold was set to obtain a defined  
1029 average activity level  $\alpha$ .

1030 **b**,  $R_{out}$  versus  $R_{in}$  plots for finite neuronal populations with different convergence–  
1031 divergence ratios. Top,  $n_{EC} : n_{GC} = 10,000 : 100,000$ ; bottom,  $n_{EC} : n_{GC} = 100,000 :$   
1032  $10,000$ .

1033 **c**, Contour plot of  $\psi$  against the number of presynaptic neurons ( $n_{EC}$ , abscissa) and the  
1034 number of postsynaptic neurons ( $n_{GC}$ , ordinate). Contour lines indicate  $\psi$ ; warm colors  
1035 represent high values, cold colors indicate low values. In all simulations, the activity  
1036 level was set to  $\alpha = 0.01$ .

1037 **d**, Plot of  $\psi$  against presynaptic–postsynaptic divergence ratio for different activity levels  
1038 (red,  $\alpha = 0.1$ ; green,  $\alpha = 0.01$ ; blue,  $\alpha = 0.001$ ).

1039 **e**, Analysis of divergence and convergence in a full-scale biologically inspired model of  
1040 the EC–DG circuit.

1041 **f**, Effects of changes in number of ECs ( $n_{EC}$ , top) and activity level in EC neurons ( $\alpha_{EC}$ ,  
1042 bottom).

1043 **g**, Effects of maximal connection probability ( $c_{EC-GC}$ , top) and width of EC–GC  
1044 connectivity ( $\sigma_{EC-GC}$ , bottom).

1045

1046

1047 **Figure 4** | Requirement for local PN–IN interconnectivity and fast IN signaling.

1048 **a**, Analysis of lateral inhibition mechanisms in a biologically inspired full-scale model of  
1049 the GC–PV<sup>+</sup>-IN circuit. To determine the effects of local connectivity, the width of  
1050 excitatory GC–PV<sup>+</sup>-IN connectivity ( $\sigma_{E-I}$ ) and inhibitory PV<sup>+</sup>-IN–GC connectivity ( $\sigma_{I-E}$ )  
1051 was varied.

1052 **b**, Effects of local connectivity on pattern separation. Summary bar graph of  $\psi$  for  
1053 different values of excitatory  $\sigma_{E-I}$  (top) or inhibitory  $\sigma_{I-E}$  (bottom) connectivity in the  
1054 network. Right bar in each bar graph (“Random”) represents uniform random  
1055 connectivity. Peak connectivity (and, if required, synaptic strength) was compensated to  
1056 maintain the total synaptic efficacy (different from Fig. 2f).

1057 **c**, Contour plot of  $\psi$  against width of excitatory E–I connectivity ( $\sigma_{E-I}$ ) and inhibitory I–E  
1058 connectivity ( $\sigma_{I-E}$ ). Peak connectivity (and, if required, synaptic strength) was  
1059 compensated to maintain the total synaptic efficacy. Asymmetry in spatial connectivity  
1060 rules enhances pattern separation, consistent with experimental observation of  
1061 narrower excitatory E–I connectivity and broader inhibitory I–E connectivity<sup>22</sup>.

1062 **d**, Distribution of axonal delay values in the network with standard parameters for  
1063 excitatory E–I (top) and inhibitory I–E synapses (bottom).

1064 **e**, Summary bar graph of pattern separation index  $\psi$  for impairment of fast IN signaling  
1065 by changes in synaptic delays at excitatory synapses ( $\delta_{\text{syn,E}}$  ; top), and inhibitory  
1066 synapses ( $\delta_{\text{syn,I}}$ ; bottom). Note that the effects of synaptic delay are more powerful than  
1067 the effects of propagation velocity (Supplementary Fig. 9a), highlighting the importance  
1068 of synaptic properties, e.g.  $\text{Ca}^{2+}$  channel–release sensor coupling distance<sup>61</sup>.

1069 **f**, Summary bar graph of pattern separation index  $\psi$  for impairment of fast IN signaling  
1070 by changes in the decay time constant of excitatory postsynaptic conductance  $\tau_{\text{decay,E}}$   
1071 (top) and the membrane time constant of the interneuron  $\tau_m$  (bottom). Interfering with  
1072 fast signaling at multiple levels of the lateral inhibition pathway consistently impairs  
1073 pattern separation.

1074

1075

1076 **Figure 5** | Contribution of hippocampal mossy fiber synapses to pattern separation.

1077 **a**, Analysis of effects of multi-layer structure of the hippocampal network on pattern  
1078 separation in a biologically inspired full-scale model of the EC–DG–CA3 circuit. To  
1079 address the effects of mossy fiber output, the GC–PV<sup>+</sup> interneuron network was  
1080 connected to a CA3 network via synapses with mossy fiber-like properties.

1081 **b**,  $R_{\text{out}}-R_{\text{in}}$  graph for the EC–DG component of the network. Same graph as shown in  
1082 Fig. 1c.

1083 **c**,  $R_{\text{out}}-R_{\text{in}}$  graphs for the DG–CA3 component of the network (top) and the entire  
1084 system (bottom) for different numbers of mossy fiber boutons per axon.

1085 **d**, Pattern separation index  $\psi$  plotted against number of mossy fiber boutons per axon.  
1086 Blue, isolated EC–DG component; red, isolated DG–CA3 mossy fiber component;  
1087 green, total EC–DG–CA3 system. In both (c) and (d), synaptic strength was  
1088 compensated to maintain the total synaptic efficacy.

1089 **e, f**, Similar plots as in (c, d), but for variation of synaptic strength of mossy fiber  
1090 synapses relative to threshold. Blue, isolated EC–DG component; red, isolated DG–

1091 CA3 mossy fiber component; green, total EC–DG–CA3 system. Inset, schematic  
1092 illustration of how presynaptic plasticity at mossy fiber synapses affects pattern  
1093 separation. Left, situation before induction of synaptic plasticity (control); right, situation  
1094 after induction of presynaptic plasticity, for example facilitation or PTP<sup>25,40</sup>. Two patterns  
1095 are efficiently separated in the absence of PTP (left), but less so after PTP induction  
1096 (right).

1097

1098

1099 **Figure 6** | Contribution of PP input to pattern computations.

1100 **a–c**, Hebbian plasticity at PP EC–GC synapses switches the network from pattern  
1101 separation to pattern completion.

1102 **a**, Schematic illustration of the model that incorporates Hebbian plasticity at PP EC–GC  
1103 synapses. Synaptic plasticity was implemented according to a Hebbian rule and a  
1104 sigmoidal relation between potentiation and the number of coincident APs (Methods). **b**,  
1105  $R_{out}$ – $R_{in}$  curve with 120% (a) and 600% (b) plasticity factor at PP EC–GC synapses. **c**,  
1106 Summary bar graph of pattern separation indices  $\psi$  for various Hebbian synaptic  
1107 plasticity potentiation factors.  $\psi$  in control conditions (100%; black) was slightly lower  
1108 than in Fig. 1, because  $R_{in}$  was computed from binary EC patterns rather than analogue  
1109 drive patterns.

1110 **d–f**, Direct PP input to CA3 pyramidal neurons (EC–CA3 input) regulates the balance  
1111 between pattern separation and pattern completion.

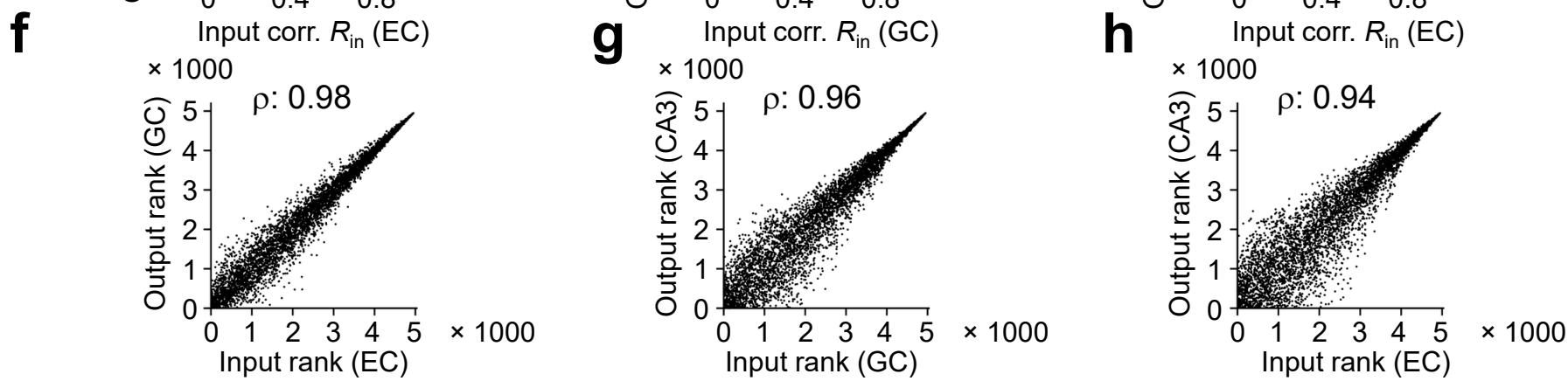
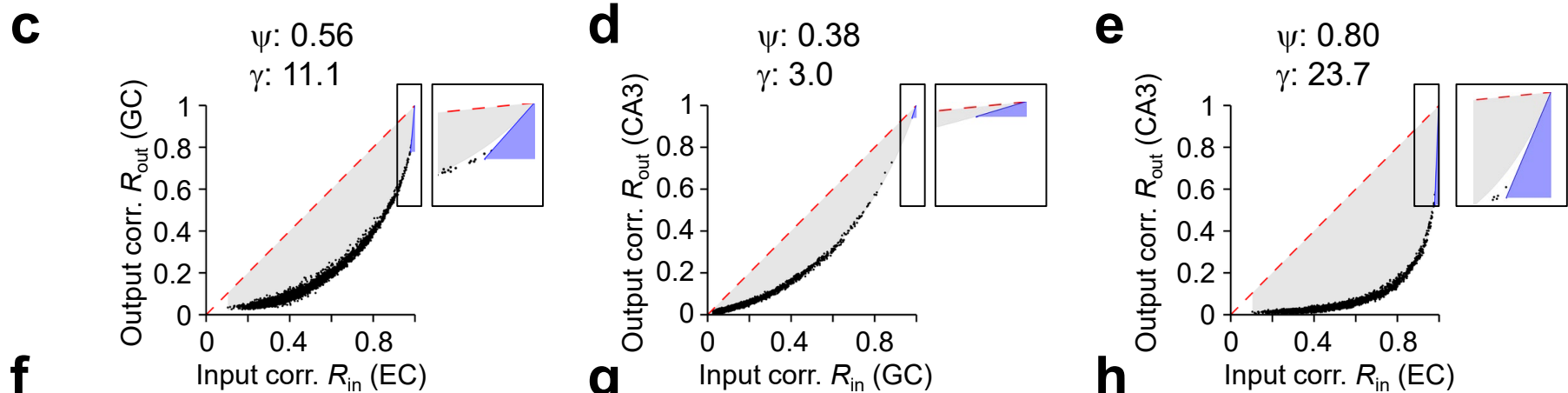
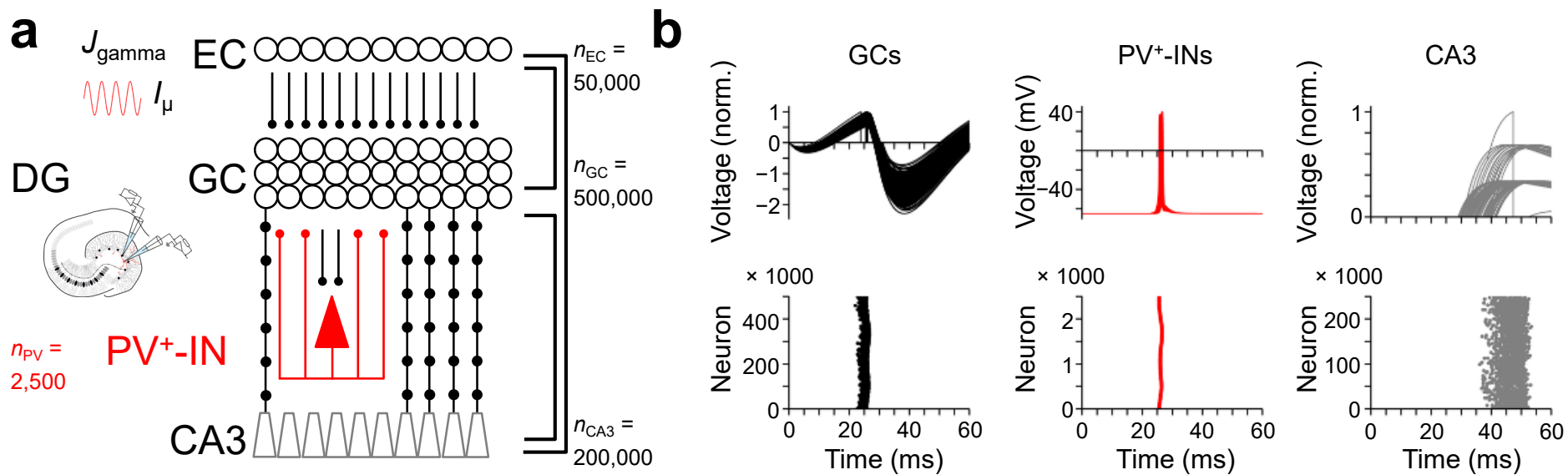
1112 **d**, Schematic illustration of the model incorporating a direct PP connection from the EC  
1113 to the CA3 region.

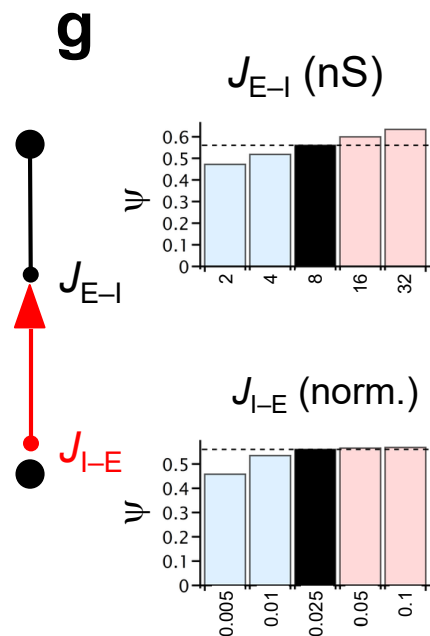
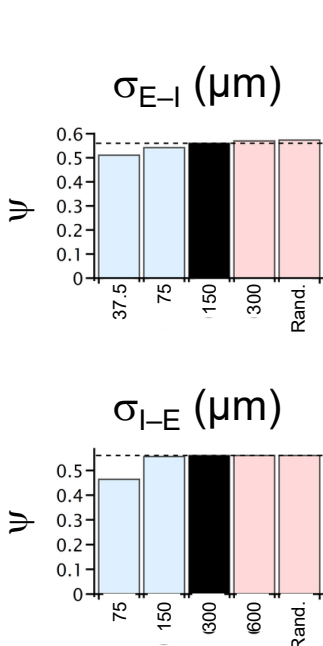
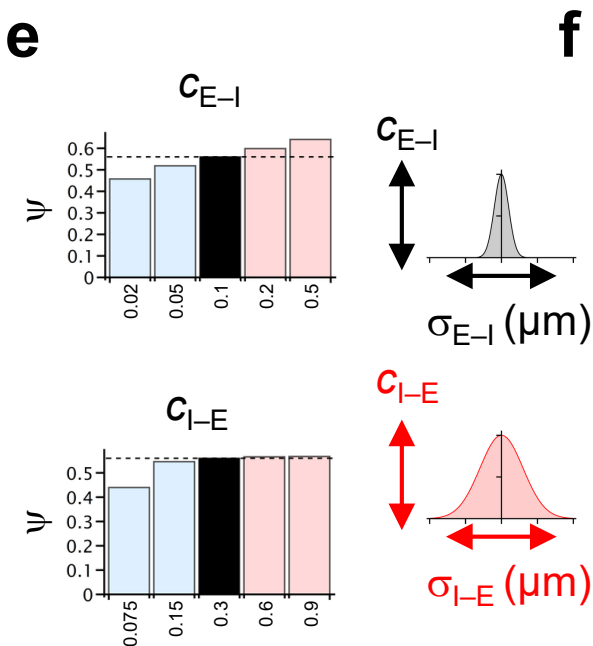
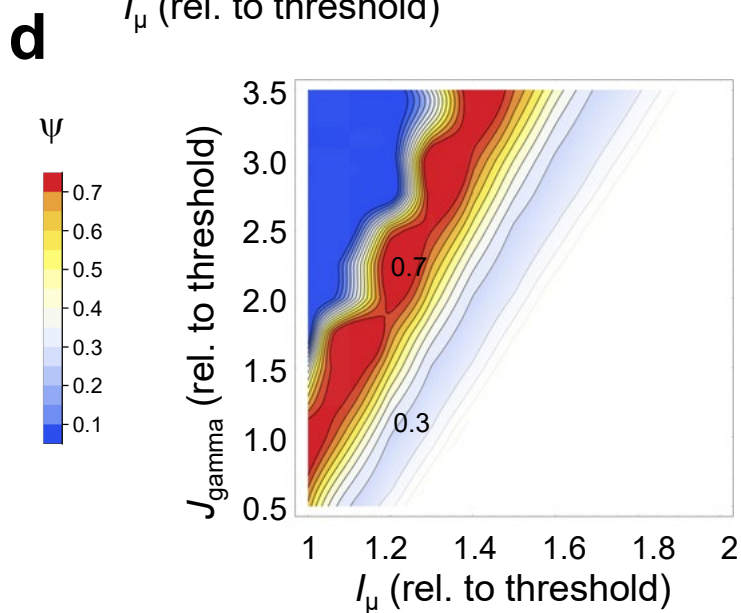
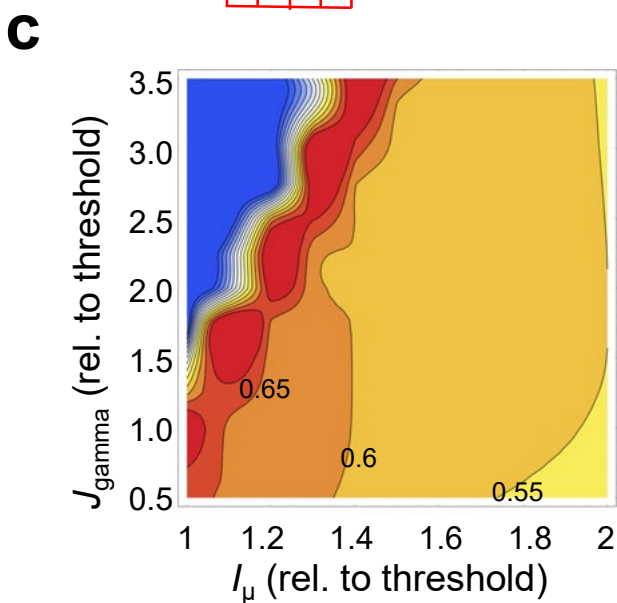
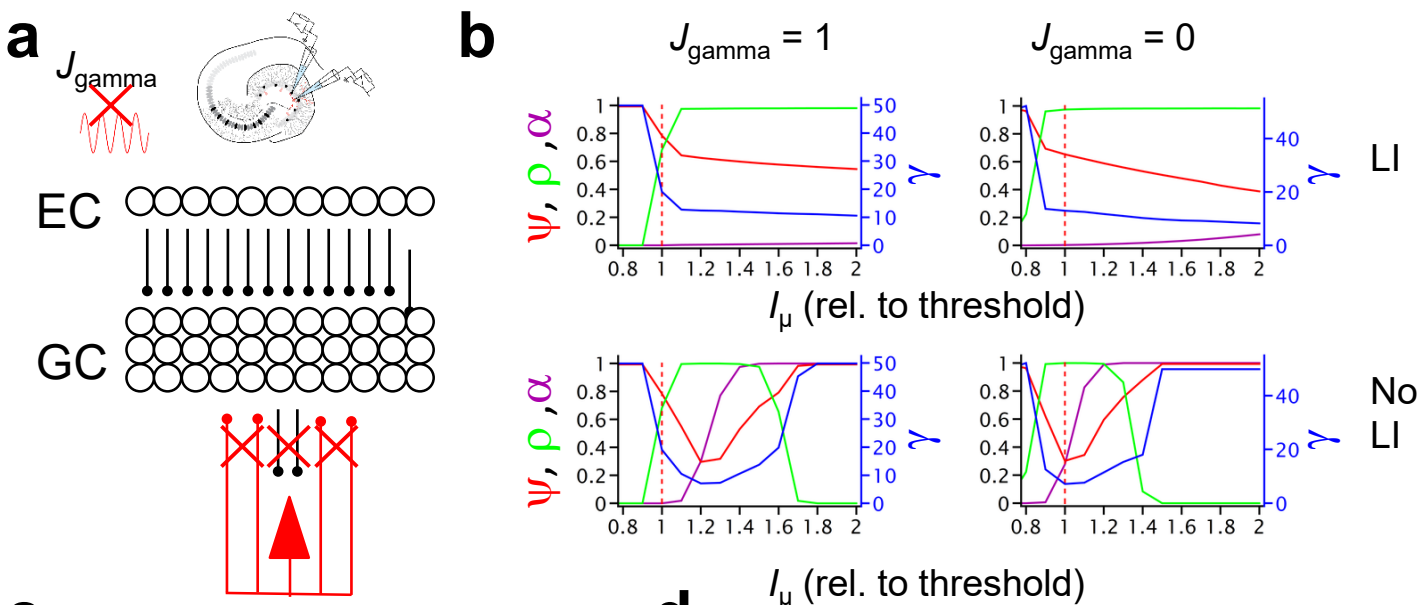
1114 **e**,  $R_{out}$ – $R_{in}$  graphs for the DG–CA3 component of the network (left) and the entire EC–  
1115 DG–CA3 network (right) for  $I_{\mu}$  EC–CA3 = 0 (top) and  $I_{\mu}$  EC–CA3 = 1 (bottom).

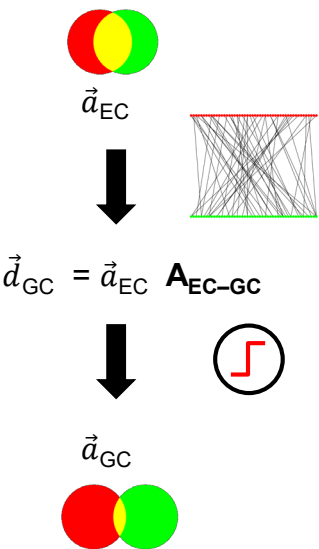
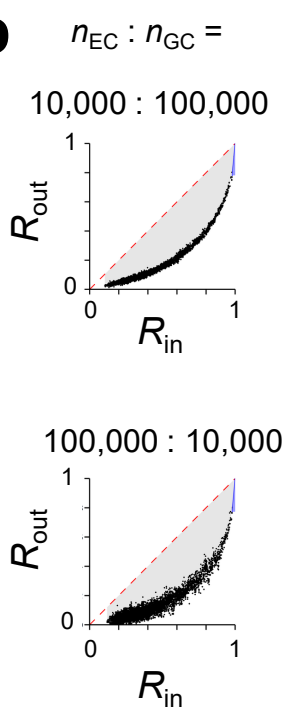
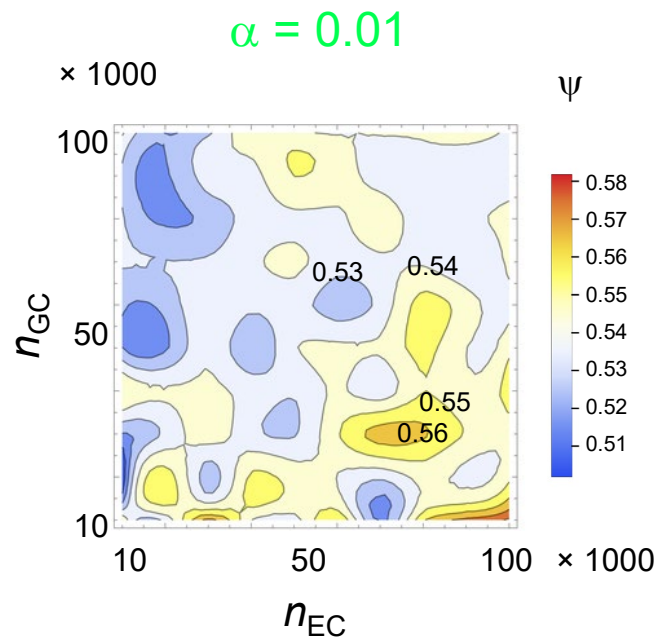
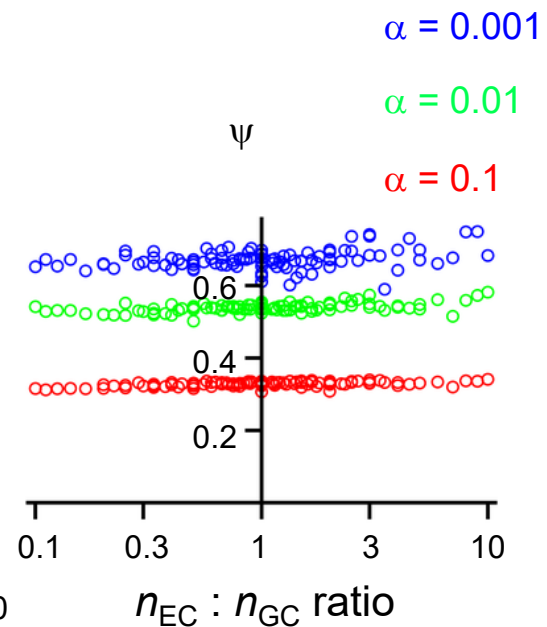
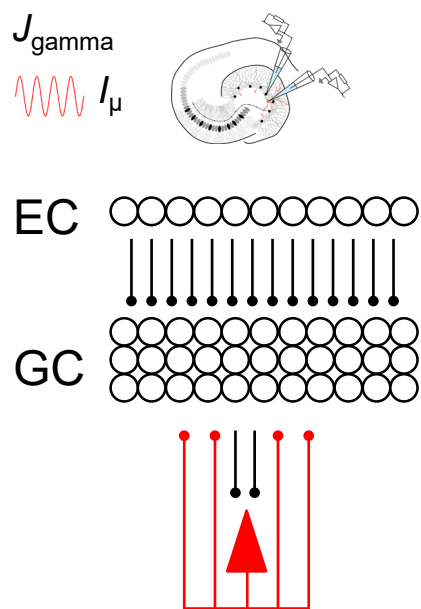
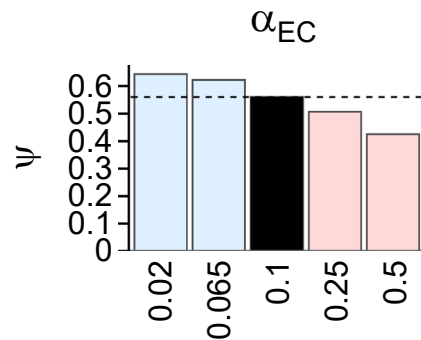
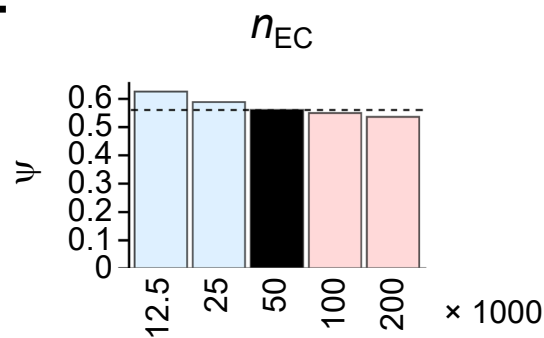
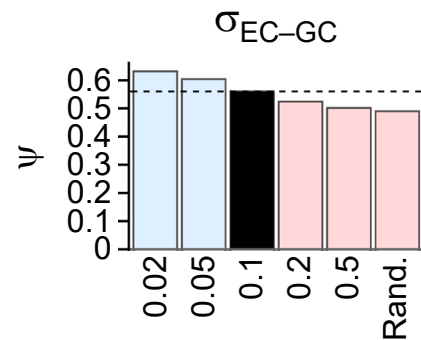
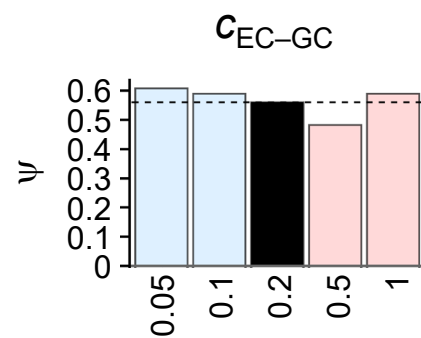
1116 **f**, Pattern separation index  $\psi$  plotted against  $I_{\mu}$  EC–CA3. Blue, isolated EC–DG  
1117 component; red, isolated DG–CA3 mossy fiber component; green, total EC–DG–CA3

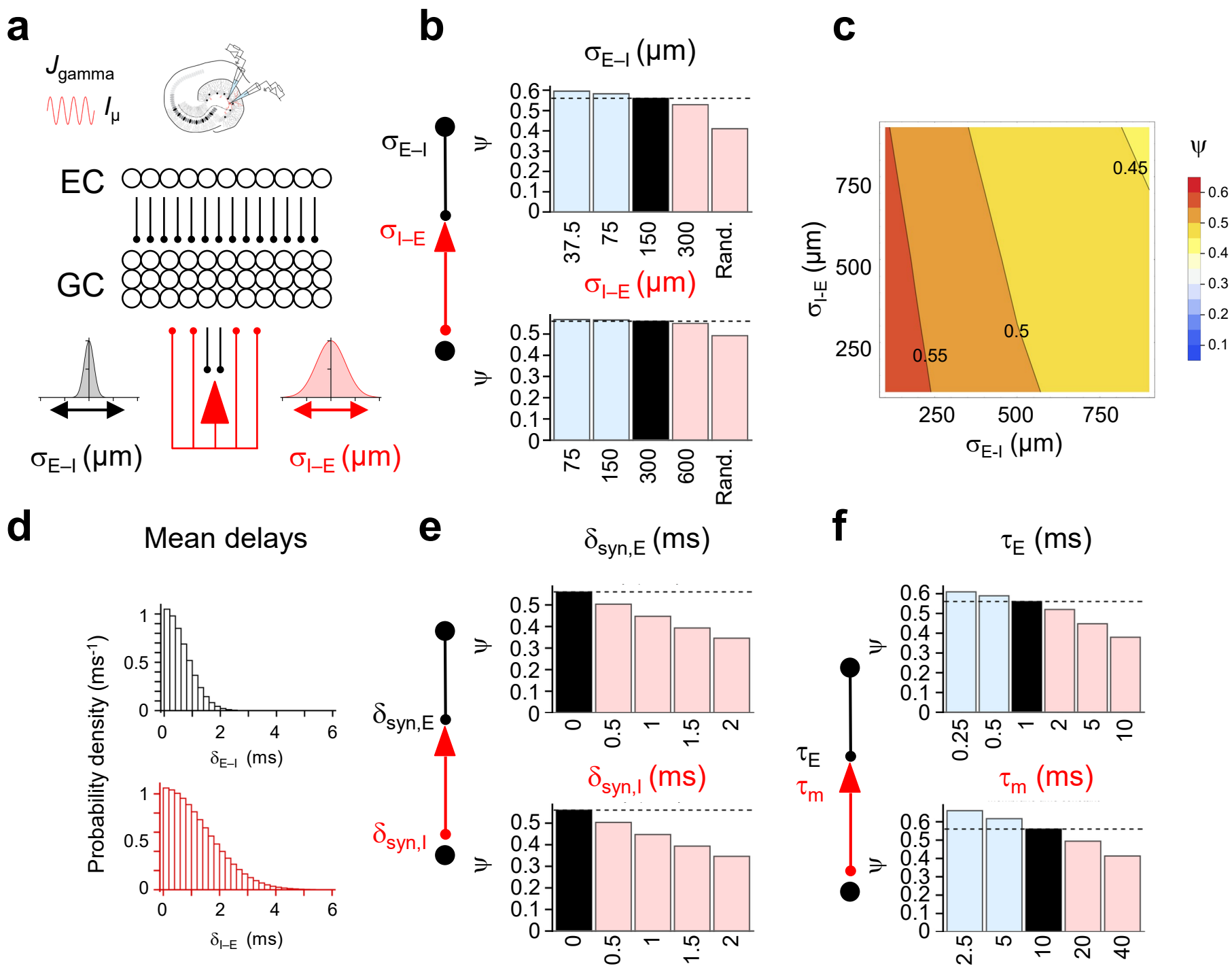
1118 system. Plateaus in the relation correspond to different integer numbers of mossy fiber  
1119 terminals required for postsynaptic spiking.

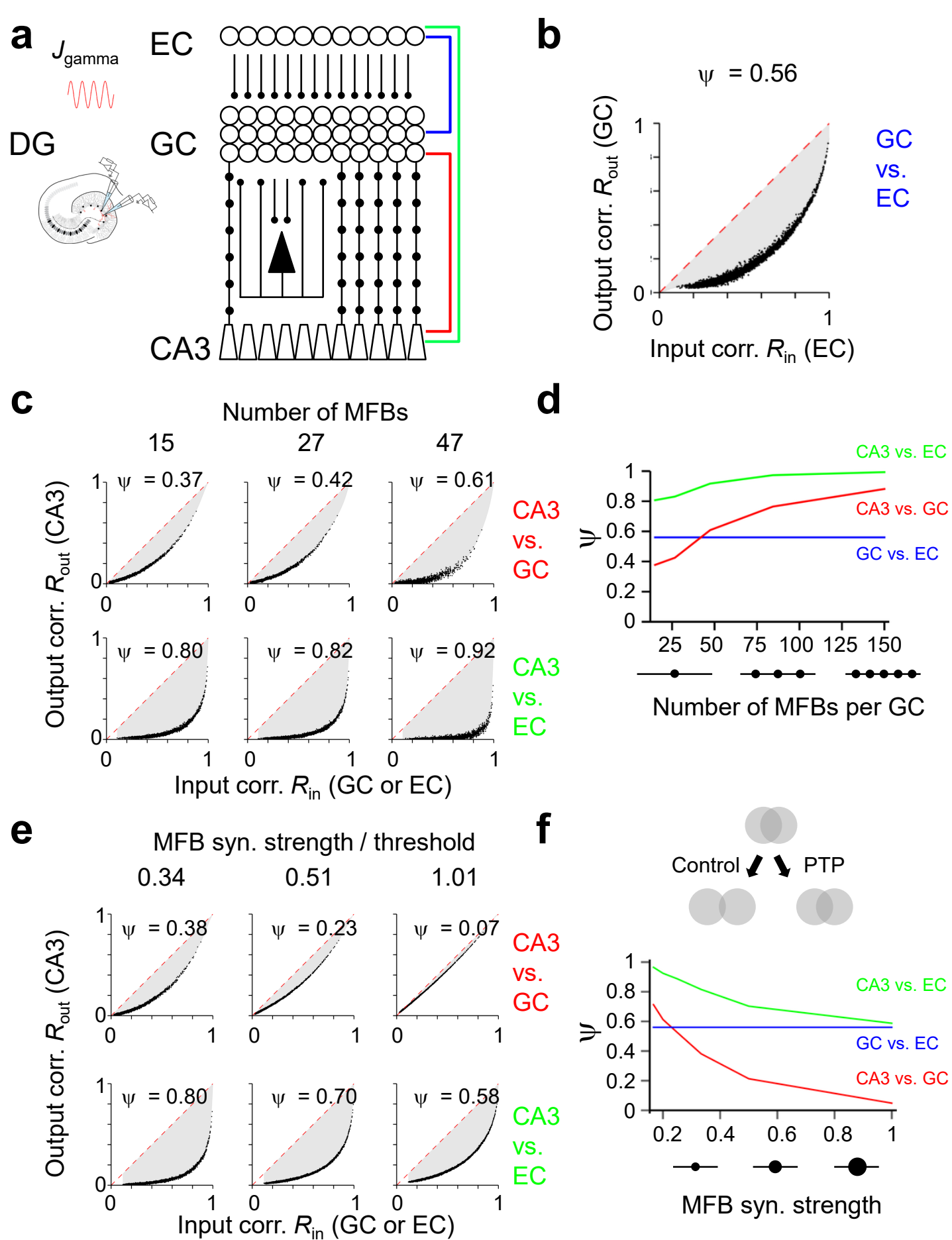
1120





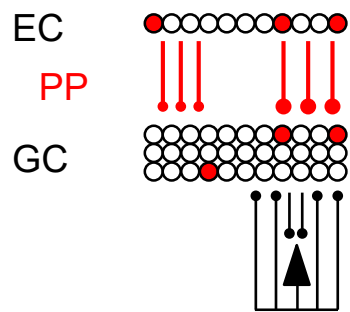
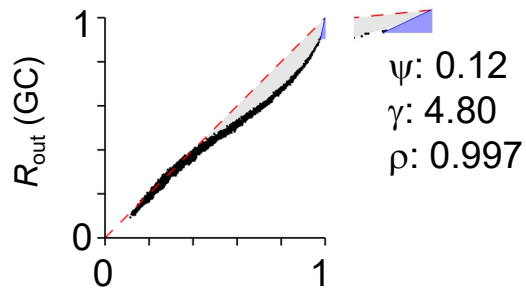
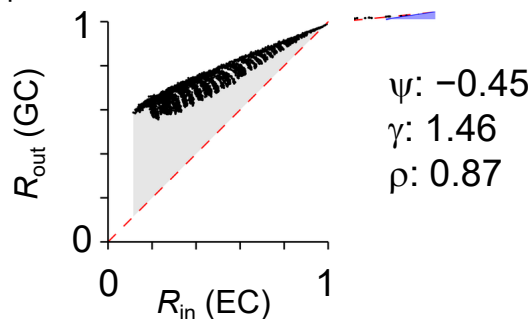
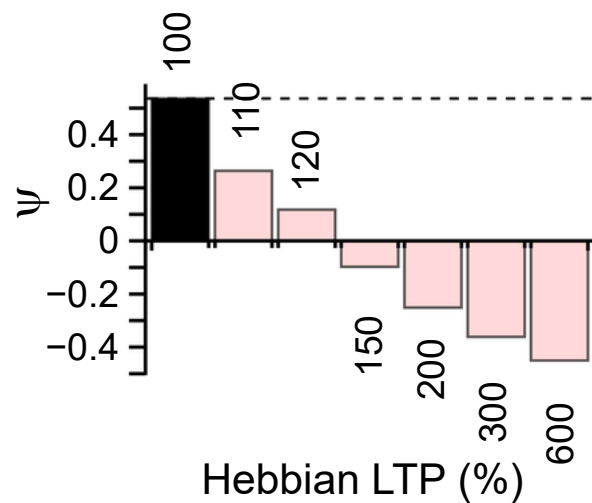
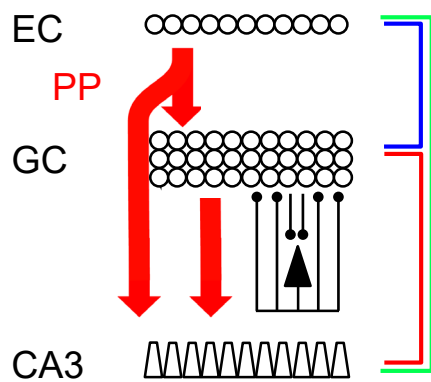
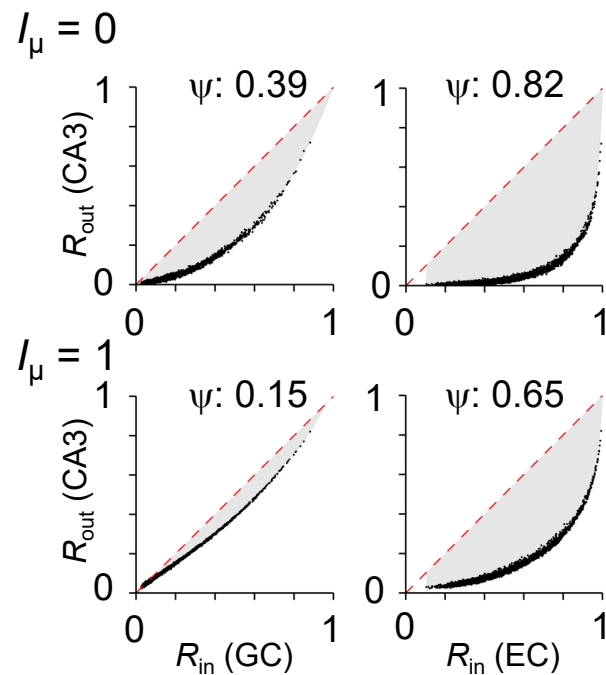
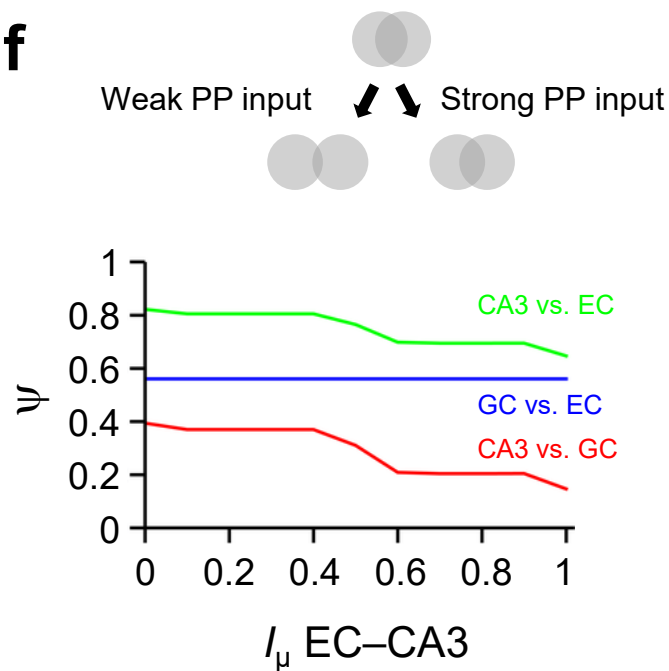
**a****b****c****d****e****f****g**





**a**

Plasticity at PP  
EC-GC synapses

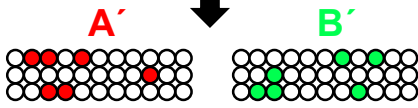
**b**
 $f_{\text{pot}} = 120\%$ 

 $f_{\text{pot}} = 600\%$ 
**c****d****e****f**

**a****A****B**

input

 $R_{in}$ 

output

 $R_{out}$ **b**

overlap

**A**  $\cap$  **B**

Cell active in context

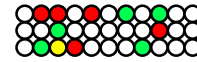
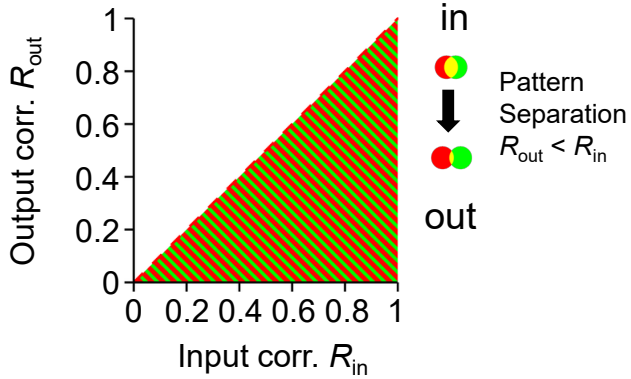
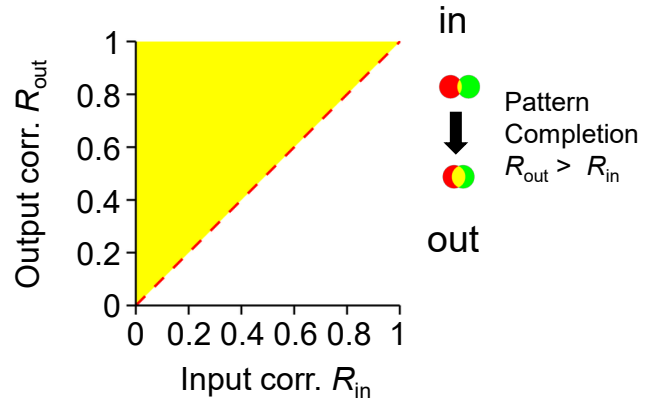
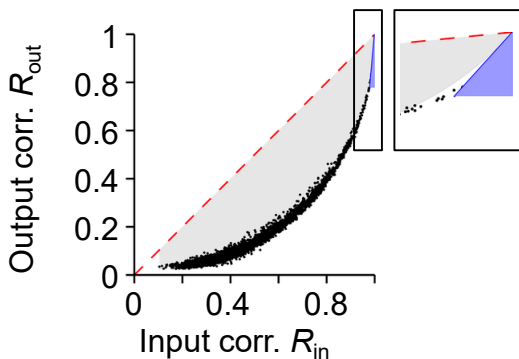
● A only

● B only

● A and B



overlap'

**A'**  $\cap$  **B'****c****d****e** $\psi$ : Normalized area between curve and IL $\gamma$ : Slope for  $R_{in} \rightarrow 1$ **f** $\rho$ : Correlation coefficient of ranks